

## Identifying Light-curve Signals with a Deep Learning Based Object Detection Algorithm. II. A General Light Curve Classification Framework

KAIMING CUI ,<sup>1</sup> D. J. ARMSTRONG ,<sup>2,3</sup> AND FABO FENG ,<sup>1,4</sup>

<sup>1</sup> *Tsung-Dao Lee Institute, Shanghai Jiao Tong University, 800 Dongchuan Road, Shanghai 200240, People's Republic of China*

<sup>2</sup> *Department of Physics, University of Warwick, Gibbet Hill Road, Coventry CV4 7AL, UK*

<sup>3</sup> *Centre for Exoplanets and Habitability, University of Warwick, Gibbet Hill Road, Coventry, CV4 7AL, UK*

<sup>4</sup> *School of Physics and Astronomy, Shanghai Jiao Tong University, 800 Dongchuan Road, Shanghai 200240, People's Republic of China*

### ABSTRACT

Vast amounts of astronomical photometric data are generated from various projects, requiring significant efforts to identify variable stars and other object classes. In light of this, a general, widely applicable classification framework would simplify the task of designing custom classifiers. We present a novel deep learning framework for classifying light curves using a weakly supervised object detection model. Our framework identifies the optimal windows for both light curves and power spectra automatically, and zooms in on their corresponding data. This allows for automatic feature extraction from both time and frequency domains, enabling our model to handle data across different scales and sampling intervals. We train our model on datasets obtained from both space-based and ground-based multi-band observations of variable stars and transients. We achieve an accuracy of 87% for combined variables and transient events, which is comparable to the performance of previous feature-based models. Our trained model can be utilized directly to other missions, such as ASAS-SN, without requiring any retraining or fine-tuning. To address known issues with miscalibrated predictive probabilities, we apply conformal prediction to generate robust predictive sets that guarantee true label coverage with a given probability. Additionally, we incorporate various anomaly detection algorithms to empower our model with the ability to identify out-of-distribution objects. Our framework is implemented in the Deep-LC toolkit, which is an open-source Python package hosted on Github<sup>a)</sup> and PyPI.

*Keywords:* Light curve classification — Astronomy data analysis — Convolutional neural networks — Variable stars — Transient detection

### 1. INTRODUCTION

A light curve (LC) is a time-dependent record of the intensity of light observed from astronomical objects. It contains valuable information about the object's properties and behavior. From an astrophysical perspective, the classification of LCs in various research fields primarily includes variable stars and transient sources.

Regarding variable star research, the classification can be quite diverse, as different types of stars exhibit their unique characteristics due to different physical processes. This offers crucial perspectives into the structure and evolution of stars. Mowlavi et al. (2018) and Gaia Collaboration et al. (2019) summarize a comprehensive known variability taxonomy tree based on the general catalog of variable stars and Gaia data. They categorize stellar variations, based on physical processes, into seven types: rotation, eclipse, microlensing, eruptive stars, cataclysmic sources, pulsation, and secular evolution. The more specific classification levels we usually use (such as eclipsing binary (EB), RS CVn,  $\delta$  Scuti, solar-like, etc.) all belong to subclasses of the above categories.

Like stellar sources, transients can also be regarded as a type of variable star with shorter time scales. According to the above classification, they should be categorized as eruptive stars. However, due to the different physical processes

cuikaiming@sjtu.edu.cn

<sup>a)</sup> <https://github.com/ckm3/Deep-LC>

behind them, and the accompanying high-energy emission across multiple bands and messengers (such as X-ray, Radio, neutrino, and gravitational wave), transients and variable stars are usually treated separately as different research areas. Some typical transients are supernovae (SNe), cataclysmic variable (CV), gamma-ray burst, tidal disruption event, and fast radio bursts, etc. In some studies, active galactic nuclei (AGN) are also classified alongside transients as extragalactic sources (Kessler et al. 2019). Due to the non-recurring nature of these events, rapid classification of transients is crucial. Immediate detection and multi-wavelength follow-up are essential for a thorough understanding of the involved physical processes.

There are several citizen science projects, such as Citizen ASAS-SN<sup>1</sup>, SuperWASP Variable Stars<sup>2</sup>, and Gaia Vari<sup>3</sup> that aim to train the public in visually classifying light curves. These projects provide simple light curves and folded light curves with some auxiliary parameters, hoping to utilize human visual perception. However, due to the accumulation of a vast amount of photometric data, machine learning has become almost the only option for rapid and automatic LC classification. Recent computer vision algorithms can outperform human eyes in most cases. In terms of variable stars, recent representative space missions such as Kepler (Borucki et al. 2010), K2 (Howell et al. 2014), and TESS (Ricker et al. 2014) provide us with unprecedented high-precision and high-duty-cycle observational data. With this data quality, variable star classification can be performed well based on their distinct features with various classical machine learning techniques (e.g., Hinnens et al. 2018; Armstrong et al. 2015, 2016; Audenaert et al. 2021). Some vision based convolution neural network (CNN) algorithms are utilized with the help of the frequency domain information, mainly focusing on asteroseismology (e.g., Hon et al. 2018a,b). Ground-based observations also supply more general scenarios for exploring new algorithms. For example, Jamal & Bloom (2020a) classify LCs with their folded LC images on Optical Gravitational Lensing Experiment data. Naul et al. (2018) employ a recurrent neural network (RNN) to alleviate the issue of non-uniformly sampled data to some extent. Jamal & Bloom (2020b) test various time series neural networks, including long short-term memory (LSTM), gated recurrent unit (GRU), temporal CNN and dilated temporal CNN.

Classifying ground-based multi-band transient LCs is a challenging task. There are many algorithms that have been applied, including some feature-based classical algorithms (e.g., Villar et al. 2019; Sánchez-Sáez et al. 2021; Förster et al. 2021; Sánchez-Sáez et al. 2023) which have achieved a high accuracy on both variables and transients from the Zwicky Transient Facility (ZTF; Bellm 2014; Bellm et al. 2018). Time series algorithms based on deep learning techniques like CNN, RNN, GRU and LSTM are widely adopted (e.g., Charnock & Moss 2017; Pasquet et al. 2019; Muthukrishna et al. 2019; Möller & de Boissière 2020; Becker et al. 2020). Attention based Transformer algorithms have been actively explored in recent years (e.g., Pimentel et al. 2022; Allam Jr. & McEwen 2023; Donoso-Oliva et al. 2023; Pan et al. 2023). There are also some methods that use a generative adversarial network (García-Jara et al. 2022), as well as direct identification of photometric image sequences using a recurrent CNN model (Carrasco-Davis et al. 2019).

As time domain surveys continue to evolve, higher cadences and larger fields of view are reducing the gap between observations of variable stars and transients. Classification algorithms also need to improve along this direction. In this work, we develop a general LC classification framework based on a weakly supervised object detection model. It can extract time domain and frequency domain features as an imitation of human behavior. Section 2 describes our dataset selection and preparation, Section 3 introduces our model architecture. Section 4 shows the training process, hyper-parameter choices, evaluation (Section 4.1) and uncertainty analysis (Section 4.2). In Section 5 we explore the anomaly detection with our model’s output features. Limitations, and future applications of our model are discussed in Section 6.

## 2. DATASET PREPARATION

A general classification framework should be able to handle different sources of data. First, space observations are typically more uniform and have fewer gaps, while ground-based observations are subject to inevitable daily windows but can offer longer baselines. Second, observation can be white light or multi-band. Third, different missions have different target selections. To cover both space- and ground-based observations, we choose Kepler and TESS as representatives of space telescope data, and ZTF as a representative of ground-based observations. To have a reliable evaluation of our model, we adopt the same training data from previous state-of-the-art works. Our Kepler training

<sup>1</sup> <https://www.zooniverse.org/projects/tharinduj/citizen-asas-sn>

<sup>2</sup> <https://www.zooniverse.org/projects/ajnorton/superwasp-variable-stars>

<sup>3</sup> <https://www.zooniverse.org/projects/gaia-zooniverse/gaia-vari>

sample is from the recent TESS data for asteroseismology classification algorithm (T'DA; Audenaert et al. 2021)<sup>4</sup>, we adopt their Kepler ID catalogue but select data from all available quarters. We obtained our TESS training samples from the visual inspection conducted by Balona (2022). After performing a sampling-based double check, we utilized the initial four years (Sector 1-55) of 2-minute data from the (Jenkins et al. 2016). Presearch data conditioned simple aperture photometry (PDCSAP; Smith et al. 2012) LCs are used for both Kepler and TESS sample. Kepler and TESS data are processed with `lightkurve` (Lightkurve Collaboration et al. 2018; Barentsen et al. 2021) and our extension (`lightkurve-ext`; Cui 2022), which is available on GitHub<sup>5</sup>. All the *Kpler* and *TESS* data used in this paper can be found in MAST: doi:10.17909/T9488N and doi:10.17909/t9-nmc8-f686. ZTF training dataset is downloaded from the automatic learning for the rapid classification of events (ALeRCE) broker Sánchez-Sáez et al. (2021)<sup>6</sup>.

Our combined training dataset is formed from those three sets, while combining their taxonomy. Since the T'DA dataset and ALeRCE dataset share some common classes, to ensure there is no conflict in their definitions, we make slight adjustments to the data. First, the aperiodic sample in the T'DA is based on the long-period variables (LPVs) detected by Yu et al. (2020) to simulate variables with period longer than half of a sector. We exclude this class as we use all available quarters, otherwise they would no longer be aperiodic and can be confused with certain rotators or pulsators without the knowledge of stellar parameters. Second, the Periodic-Other sample in ALeRCE dataset is a catch-all type class, summarizing periodic variable stars without a clear label. However, this can cause confusion with some classes in T'DA dataset, so it's excluded in our dataset. Then, because the 'Constant' type in T'DA is only designed for TESS, we develop a new class named 'Random', which purely generates white noise. This noise flux follows a normal distribution  $\mathcal{N}(0, \sigma)$ , and the  $\sigma$  follows log-uniform distribution  $\mathcal{LU}(-6, 1)$  with base 10. The noise time cadences are sampled uniformly between 1 minute and 2 hours, and the time span uniformly from 10 to 1400 days.

We also possess an additional dataset of variable stars that solely contain data from Kepler and TESS. This dataset is created to facilitate a comparison with the performance of T'DA. Finally, our combined dataset contain 17 different classes, with a total of 24,552 objects and they are summarized as Table 1. The variable star dataset consists of the first 7 classes. Since we do not want to emphasize either variables (Kepler/TESS) or transients (ZTF) data, we under-sample certain classes to maintain a nearly equal size of the ZTF and Kepler/TESS datasets while avoiding a reduction in less frequent categories. Usually variable stars are easier to classified, more variables can bias our performance and less total sample size can save our training time significantly. We do not employ any imbalanced learning technique to over-sample less represented classes, as it may not always be beneficial and could potentially harm our model's calibration (Elor & Averbuch-Elor 2022). The training and test datasets are divided at a ratio of 80% and 20%, respectively. The validation dataset is made by 5-fold cross validation from the training data. Note our sample is mainly designed for maintaining consistency with previous work, more complete samples from different missions and simulations can be collected in the future (see Section 6).

To explore the distribution of our dataset and also investigate the difficulty level of classification, we train a Self-Organizing Map (Kohonen 1990, SOM;) model to our training dataset. We use the folded LC based on the most significant frequency, following the methodology of Armstrong et al. (2016). The typology of folded LC features in our sample is shown in Figure 1 using trained SOM results. While some labels, such as EB and RRL, can be easily classified and set apart from others, most classes do not display a clear distinction. This demonstrates that a simple phase-folded LC is insufficient for classifying all these diverse classes.

### 3. CLASSIFICATION FRAMEWORK

An ideal scenario for time series analysis is to have a network that utilizes a single algorithm capable of extracting all relevant information from both the input time series data points and the input sample distribution. With such a network, it would be possible to complete all tasks related to time series analysis in an end-to-end manner. However, even sophisticated Transformer models have not managed to surpass the performance of straightforward linear models on some real-life dataset (Zeng et al. 2022). Furthermore, enhancing or integrating traditional algorithms can potentially lead to superior outcomes (Sun & Boning 2022). Instead of relying on a single time series model, our model

<sup>4</sup> <https://github.com/tasoc/starclass>

<sup>5</sup> <https://github.com/ckm3/lightkurve-ext>

<sup>6</sup> <https://zenodo.org/records/4279623>

**Table 1.** Summary of the dataset

Class	Number ( $N_{\text{Kepler}} + N_{\text{TESS}} + N_{\text{ZTF}}$ )
Rotation or Contact EB (Rot/CEB)	4113(2260 + 1853 + 1000)
$\delta$ Scuti or $\beta$ Cephei Stars ( $\delta$ Sct/ $\beta$ Cep)	3057(772 + 1553 + 0)
$\gamma$ Doradus or Slowly Pulsating B Stars ( $\gamma$ Dor/SPB)	1746(630 + 1116 + 0)
Random	1000
RR Lyrae or Cepheid Stars (RRL/Cep)	1855(43 + 194 + 1618)
Solar-like Pulsators (Solar-like)	1811(1800 + 11 + 0)
Eclipses or Transits (EB/Transit)	1974(974 + 0 + 1000)
AGN	1000(0 + 0 + 1000)
beamed jet-dominated active galactic nuclei (Blazar)	1267(0 + 0 + 1267)
CV/Nova	871(0 + 0 + 871)
LPV	1400(0 + 0 + 1400)
type 1 quasar (QSO)	1000(0 + 0 + 1000)
super luminous supernova (SLSN)	24(0 + 0 + 24)
SN II	328(0 + 0 + 328)
SN Ia	1272(0 + 0 + 1272)
SN Ibc	94(0 + 0 + 94)
young stellar object (YSO)	1740(0 + 0 + 1740)

integrates domain knowledge. This will allow the designing of distinctive feature extraction modules tailored to the physical properties of each category.

Inspired by previous work on visually fine-grained classification and validation of LCs (e.g., [Balona & Dziembowski 2011](#); [Gaulme & Guzik 2019](#); [Twicken et al. 2018](#)), the starting point for classification is usually the morphology of LCs at different time scales, as well as frequency domain information and some auxiliary physical parameters. Thus, unlike most time series models, a general model should utilize time-domain, frequency-domain and physical parameters all together. Additionally, it must possess the capability to independently manipulate or process data in order to adapt to varying data scenarios. Most classification models that use LCs as input are usually designed for specific missions, with predetermined lengths of LC inputs, known observation cadences and colors. To enable our model to handle such diverse inputs, we apply various techniques to mitigate this issue.

First, in order to allow the model to handle variable-length and non-equal-interval sampled sequence data, we convert the LC to images, together with the original LC data, to serve as the input for the network. This approach has several advantages. Initially, models for 1D time series such as 1D CNN require a fixed shape and other models like RNN and LSTM have limited perception range, making them difficult to process inputs spanning multiple orders of magnitude (such as TESS’s 2-minute cadence 27.4 day observations and daily ground-based long term observations). Previous preprocessing techniques such as binning, padding, and interpolation can alter the flux information for different time scales or result in redundancy. However, for 2D images, the data size remains unchanged while the flux and time range information is not affected by resolution. Additionally, observation data from different bands can be naturally represented by different colors without any requirement for data size and time alignment. Moreover, image data also allows us to fully utilize well-established 2D CNN models that are widely used in computer vision applications. Some studies also apply this method for LC or sequential data analysis, which benefit from fixed-size inputs and leveraging existing 2D CNN algorithms. (e.g., [Hon et al. 2018b](#); [Jamal & Bloom 2020a](#); [Cui et al. 2022](#)). Furthermore, converting time series into images can be regarded as a type of prior data augmentation that integrates human perception. This approach is highly intuitive and facilitates the interpretation of model outcomes. However, since images only provide compressed representations at certain scales, the data input accepted by models is severely affected by factors such as image size and resolution. Therefore, we have to integrate zooming capabilities into our model to allow for analysis at smaller scales, simulating human behavior in LC classification.

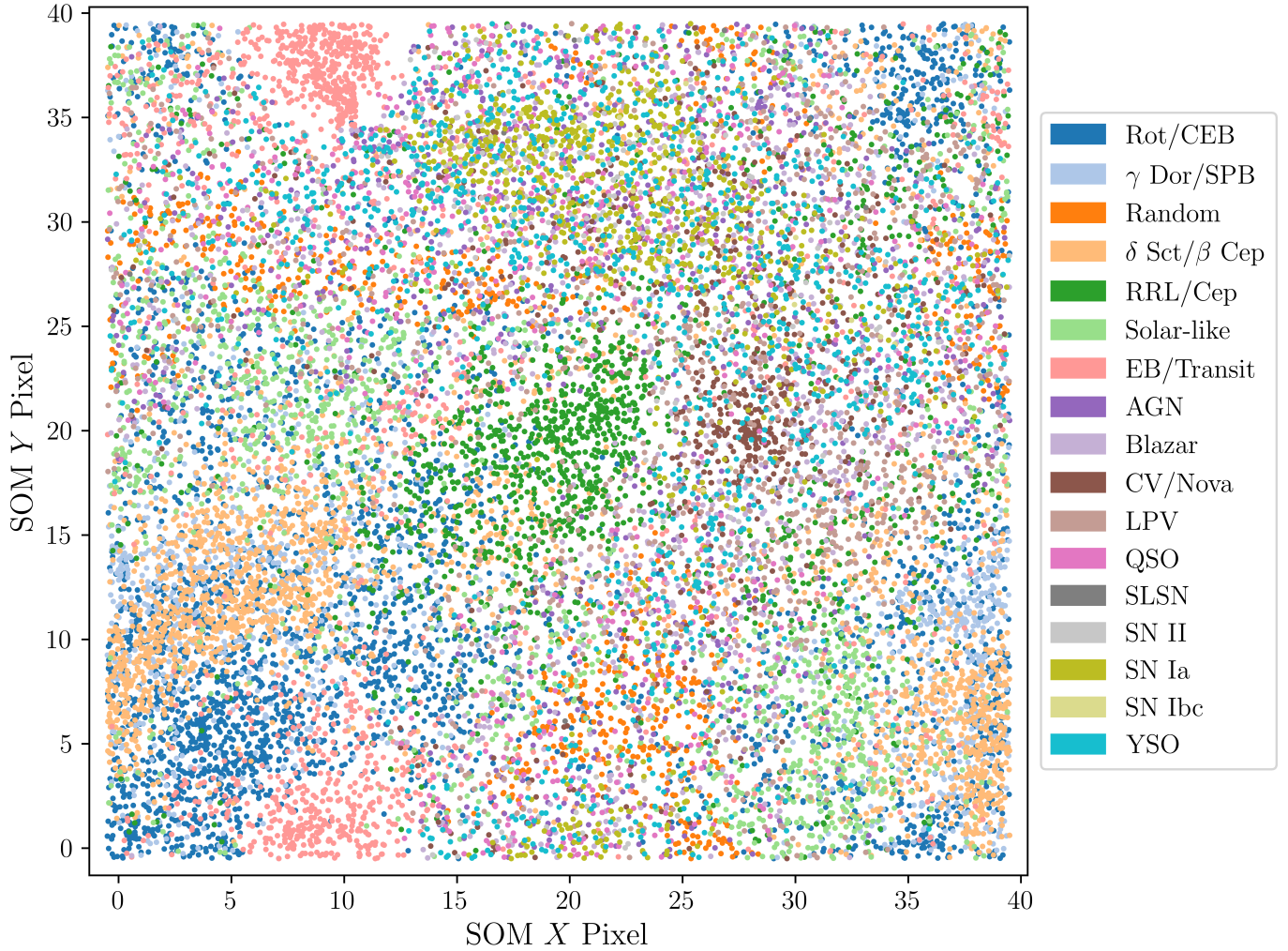


**Figure 1.** SOM 2D representation of the training dataset.

Developing a neural network algorithm with the ability to zoom is tough because it requires the network to have the capability of perception and action. For the perception, experiments show that different layers of the CNN model will activate corresponding features for the target, which is also the basis of object detection algorithms (Zeiler & Fergus 2014). Based on activation regions from feature maps, reinforcement learning seems like a straightforward approach for learning how to perform zooming operations. This involves rewarding or penalizing the network's zooming behavior based on classification results in the zoomed region (e.g., Gao et al. 2018). However, we find that reinforcement learning is difficult to converge in our classification task. The main reason could be due to challenges in establishing a relationship between reward function and classification scores. Additionally, due to the sparsity of the action space, the efficiency of the parameter updating is low, leading to decreased training efficiency.

Another option is weakly-supervised object detection methods, which detect and localize instances with solely image-level classification labels (Shao et al. 2021). In this work, we adopt the algorithm from a fine-grained classification and object detection model called Navigator-Teacher-Scrutinizer Network (NTS-Net; Yang et al. 2018). This model employs a weakly-supervised learning technique to achieve simultaneous classification and detection. The main process of this algorithm involves using a navigator network to propose regions of interest from the image, and a scrutinizer network to extract features from the regions and make predictions. The navigator and the scrutinizer work together in an iterative manner, refining the regions of interest and improving the accuracy of the detection, and better detection returns higher classification scores. The navigator network applies anchor boxes and a region proposal network (RPN; Ren et al. 2016) as an object detector, and the scrutinizer network adopts a pretrained CNN model as the basic feature extractor. The model's primary loss is composed of a few distinct losses: the cross-entropy loss, which serves

as the fundamental loss for classification, is applied to the raw LC, zoomed LCs, and final combined data; a rank loss is applied to align the sorting of the output scores from the region proposal network with the sorting of the correct classification logits. By doing so, the network achieves a weakly supervised object detection process.

After implementing the zooming capability in our model, it can effectively analyze LCs of different scales and determine appropriate scales for classification. Figure 2 illustrates the structure and process of our model, which includes a LC component responsible for feature extraction from LC images and zooming in on LC data. The final label prediction is generated by integrating both raw and zoomed-in LC data. We have also implemented a similar process for the power spectrum (PS), which is calculated with a Lomb-Scargle algorithm (Lomb 1976; Scargle 1982), allowing it to accommodate PS with various frequency resolutions and ranges. The minimum frequency is two times of Rayleigh resolution ( $1/\Delta T$ , where  $\Delta T$  is the time length), while the maximum frequency is the Nyquist frequency, calculated based on the minimum cadence. The frequency is over-sampled by a factor of five. Slightly different from the LC component, in the PS component, we used the zoomed region to identify significant frequencies and then fold the original LC according to these frequencies. We combined the folded LCs with the original spectrum for the final classification prediction. In fact, for the PS component, this is a more efficient approach because unlike with a LC, the specific frequency (location information) holds great importance and does not have shift invariance like LC. These two components share the same input of LC and can work independently or together for comprehensive analysis. The intermediate classification results obtained from scaling by the model can also be outputted to understand the classification process of the model. In addition to these two components, Figure 2 also displays the parameter component, which can accept pre-determined astrophysical parameters to make finer classifications. We also show the design of the spectrum/SED component; by applying similar techniques, our model will have the potential to expand to more types of astrophysical observation data. Two additional intuitive animations that demonstrate zooming and classification for both the LC and PS components are accessible on our package’s website <sup>7</sup>.

During the implementation of our model, we extensively modified NTS-Net to suit our LC classification task. First and the most direct adjustment is zooming on the 1D time series to ensure no loss of information compared with the 2D image cropping. Secondly, relying solely on ResNet classification for images is insufficient. To enhance the model’s understanding of LC with varying time scales, amplitudes, and sampling rates, necessary information such as the total time length, maximum variability, and minimum cadence are incorporated into fully-connected (FC) layers as vectors. They are acting like coordinates of a LC, essential for a model to understand LCs with different time scales, amplitudes, and sampling rates. LCs are normalized with  $(f - \text{med}(f))/|\text{med}(f)|$ ,  $f$  is the flux and  $\text{med}$  is the median function, so that relative variability can be directly extracted. Third, in contrast to image resizing, our zooming only requires manipulation in the time dimension, therefore, we replace the 2D anchor boxes with 1D anchor scales. Moreover, even after applying non-max suppression (Neubeck & Van Gool 2006) on an image level, it is still possible for a LC or PS to return duplicate regions. Thus we further detect and remove duplicate LCs or PS from the candidate regions proposed by RPN. To achieve a balance between computational cost and classification accuracy, we utilize a relatively lightweight ResNet-18 (He et al. 2015) model as the backbone for feature extraction and image classification. LC and PS are both 1D sequence data, but they exhibit distinct classification characteristics. When using RPN to provide candidate zooming regions, LC and PS require different strategies for region generation.

LC sample contains data points and time lengths spanning several orders of magnitude, so there should be more scaling sizes of region candidates to cover different time scales, but the specific times to zoom to do not need to be accurate. In contrast, PS data requires accurately covering significant frequencies by region candidates, while the scaling size can be lenient because subsequent folding operations only require the most significant local frequencies. Previous experiments observe that the shallow layers of a CNN model primarily respond to edges and textures, whereas deeper layers exhibit more class-specific semantic information (Zeiler & Fergus 2014). Thus to optimize the performance of object detection in both LC and PS components, we propose different RPNs as illustrated in Figure 3. Specifically, the RPN for LC component only uses the final feature layer of ResNet, while the RPN for PS component utilizes the last four layers to construct a feature pyramid network (FPN; Lin et al. 2017). As a widely adopted approach to enhance accuracy in object detection tasks, FPN can fuse lower and higher-level features to assist in accurately locating frequencies on our PS data. In our implementation, we have predetermined anchor regions for the LC and PS components. For each pixel of the RPN feature map in the LC component, there are nine anchor regions ranging

<sup>7</sup> <https://github.com/ckm3/Deep-LC>

from 32 to 384 pixels. In contrast, for each RPN feature pixel in the PS component, there are four anchor regions with scales ranging from 0.1 to 0.4.

In addition, we have a few limits for region selection. In the LC component, same as Sánchez-Sáez et al. (2021), when the selected LC has less than 6 data points, the selection is ignored. In the PS component, we calculate the false alarm probability (FAP) levels on the whole PS and discard regions with FAP levels lower than 1% in subsequent processes. For multi-band observations, bootstrap simulation is required to calculate FAP and this process is computationally expensive. Therefore, it has been disabled in our ZTF dataset but can be enabled in the inference with our package. For observations with large gaps, we aim to limit the model’s focus to regions with more data points. To achieve this, we introduce a new loss function that penalizes network outputs for blank areas only. This is expressed in Equation 1.

$$L_0 = \mathbb{1}^{<0} \left( \frac{1}{N_{\neq 0}} \sum_{i=0}^{N_{\neq 0}} S_i \mathbb{1}_i^{\neq 0} - \frac{1}{N_0} \sum_{i=0}^{N_0} S_i \mathbb{1}_i^0 \right) \quad (1)$$

The  $S_i$  is the score given by the RPN,  $N_0$  and  $N_{\neq 0}$  are the number of candidate zoomed regions with blank and non-blank regions,  $\mathbb{1}_i^{\neq 0}$  and  $\mathbb{1}_i^0$  are Heaviside step functions for non-zero and zero regions, respectively.  $\mathbb{1}_i^{\neq 0}$  equals to 1 when the  $i$ -th region is not blank, else 0;  $\mathbb{1}_i^0$  equals to 1 when the  $i$ -th region is blank. The  $\mathbb{1}^{<0}$  selects the loss less than 0, making sure the gradient is only back propagated to the blank areas.

Therefore, the final loss function of our LC or PS component is in the form of Equation 2.

$$L = L_C + L_S + L_{\text{ResNet}} + L_{\text{Rank}} + L_0 \quad (2)$$

The  $L_C$  is the loss function of the final combined layer, the  $L_S$  is the loss function from the scrutinizer part, which combines the LCs or PS from the proposal regions.  $L_{\text{ResNet}}$  is the initial loss from the raw images. The above three loss functions all use cross-entropy losses to minimize the differences between the predictions and ground-truth labels.  $L_{\text{Rank}}$  is the rank loss can be expressed as  $\sum_{(i,s):C_i < C_s} (I_s - I_i)$ , where  $f$  is a hinge loss function  $f(x) = \max\{1 - x, 0\}$ , and  $I$  is the RPN score,  $C$  is the predicted corresponding class logit, the opposite order of  $i$  and  $s$  under  $C$  and  $I$  plays a role in sorting. Thus, this pair-wise ranking loss can guide the navigator network to find the most helpful order for the classification results. The weights of the losses can be adjusted, but for simplicity and efficiency in hyper-parameter tuning, we have set them to be equal as there is no significant difference in their contributions to the model.

#### 4. TRAINING AND EVALUATION

Our model contains numerous hyper-parameters, which can be categorized into three types: those from the model (e.g., number of proposal regions), those from the data (e.g., image size), and those from the training process (e.g., learning rate). We employ different strategies to optimize these parameters. For the model’s hyper-parameters, the graphics processing unit (GPU) memory usage and training time is a crucial limit for number of proposal regions and anchors, only 2–10 proposal regions are possible to fit in the 40 GB memory of a NVIDIA A100, and more anchors require more central processing unit (CPU) time and CPU-GPU communication overhead. We also tried the distributed parallel training on multiple cards, but observed a significant decrease in performance. Thus, we tune these parameters within the constraints of available resources. Other models’ hyper-parameters are also hard to constrain very precisely, such as the number of RPN layers, convolution kernel sizes and number of anchors. These parameters are typically either picked by previous experiences (Mishkin et al. 2017; Lin et al. 2017; Yang et al. 2018) or tuned through trial and errors.

For the data’s hyper-parameters, they are both constrained by CNN model and prior visual check. When selecting the input image size for LC and PS, we increase the image size along both the time and frequency dimension, because the zooming regions are proposed within them. Since most CNN models are not optimized for large image sizes, we adopt the common sizes (e.g., 112, 128, and their multiples of 2 or 4) following most downstream works of ResNet. Another preset prior treatment with some hyper-parameters is our image plotting algorithm. We implement algorithms for drawing 1D sequence data to 2D images for LC and PS separately, scatter points are mapped in a 2D array directly for LCs, while line connections are drawn with Bresenham’s line algorithm (Bresenham 1987) for PS. Without using any visualization package, pure matrix operation makes our drawing fast. The size for points are 5 pixels and we use different sizes and gray scales for multi-band data.

For the hyper-parameters of the training process, we adjust them with 5-fold cross validation from our training dataset. To save tuning time, we only conduct tests on the variable star dataset. Our performance metric is the

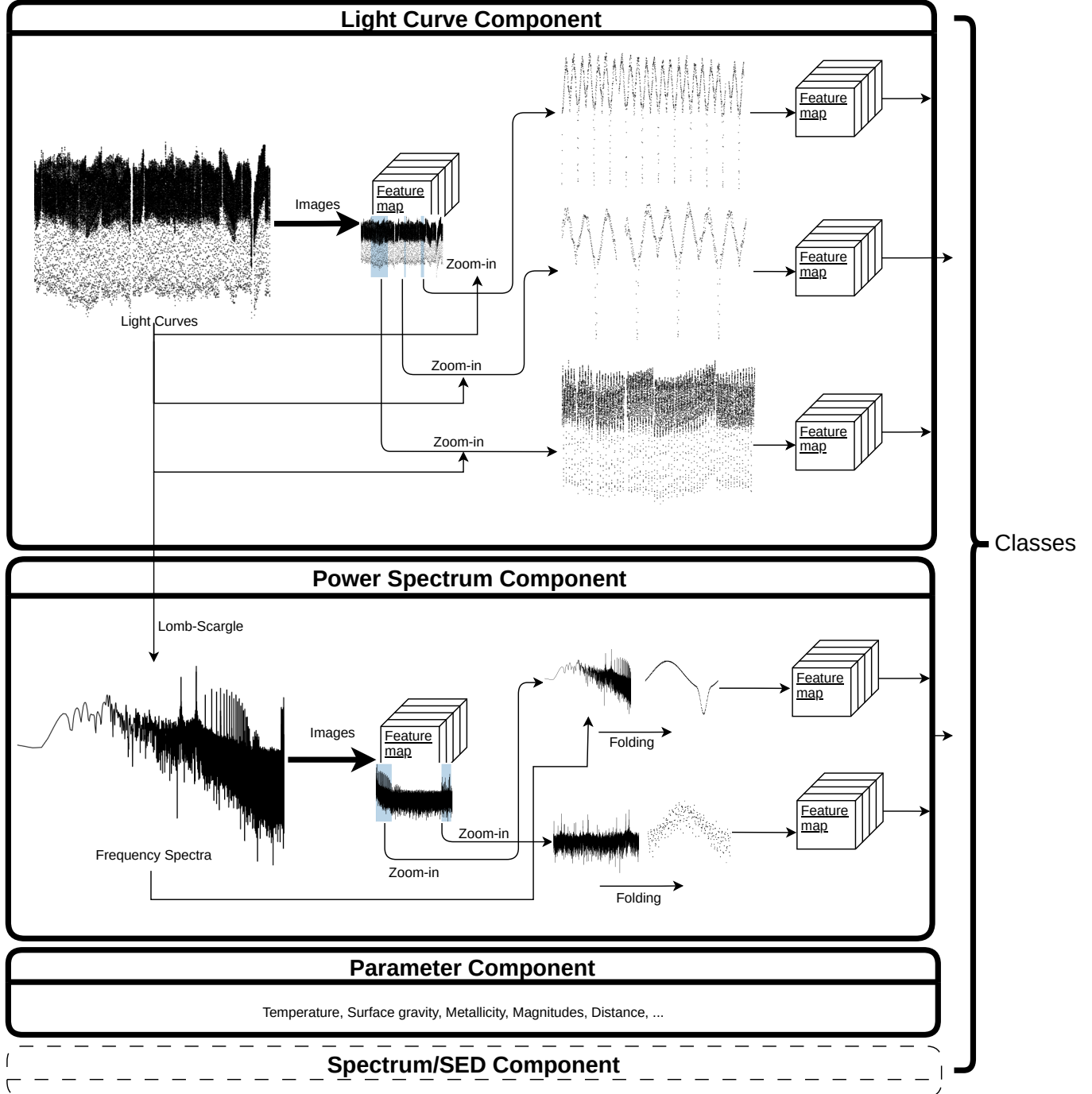


**Figure 2.** Network schematic diagram of our model. The diagram shows three main components, which are enclosed by thick black lines. Top of these components is the LC component, which has two inputs: raw LC data and image data of plotted LCs. A CNN model extracts feature maps from the images and zooms in on the input LC based on these feature maps. Then, the zoomed-in LCs enter into the same CNN model to extract features again. Finally, all features extracted from both CNN models are combined to make a prediction for the class label. The PS component receives the LC from the LC component and calculates a Lomb-Scargle periodogram as input for the network. Similar to the LC component, the frequency spectra and their images are feature extracted and zoomed in to smaller regions. Then, with the most significant frequencies in the zoomed-in regions, we can fold the LCs into folded LCs, which are then used by a CNN model to extract features. The predictive labels are generated by combining all of the features produced by these CNN models. The parameter component utilizes all manually selected physical or systematic parameters to make higher-level predictions. The optional spectrum or SED component demonstrates the potential for extensibility to additional astronomical products.

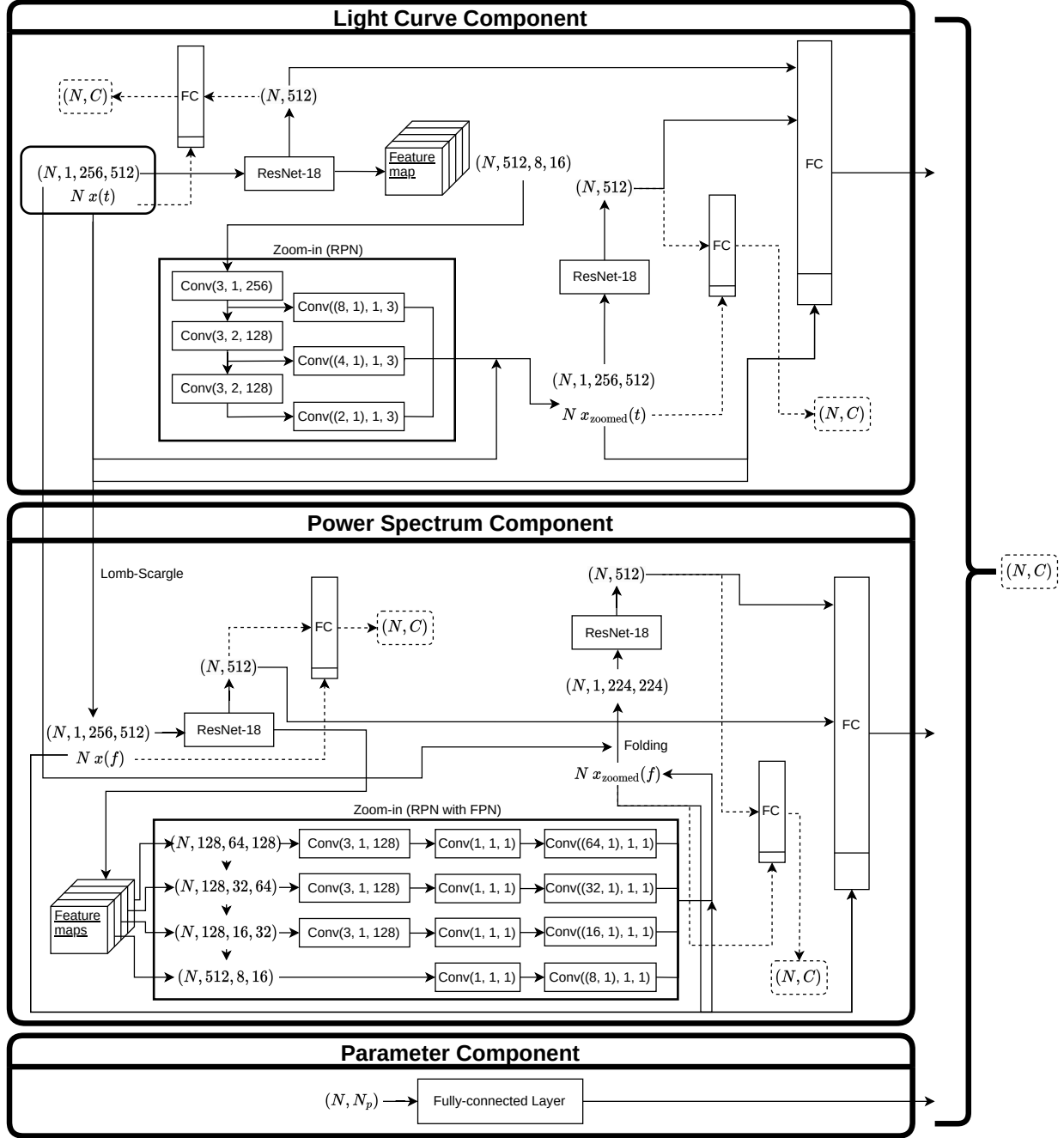


**Figure 3.** Details of the network structure’s implementation, as depicted in Figure 2. The LC component comprises the input for  $N$  LCs ( $x(t)$ ) and images, as illustrated within the solid rounded rectangle. Initially, a ResNet-18 model as the backbone for classification. The ResNet generates feature maps both with and without spatial information. Here,  $N$  represents the batch size, while 512 is the channel size following the final convolution layer. We then merge the output ( $N, 512$ ) feature map with basic LC features, routing them to a FC layer for class prediction. The FC layer is split into two sections, with the lower portion representing the input of three basic LC features, and the upper portion signifying the input feature map. ResNet’s spatial feature map output, with shape ( $N, 512, 8, 16$ ), serves as the input for the RPN (thick rectangular box region), alongside the input LC used to zoom in the LC. The numbers in a convolution block show the size, stride and number of output channels. For brevity, we only display one zoomed-in LC. Similar to the initial classification, the zoomed-in LCs ( $x_{zoomed}(t)$ ) and corresponding images are transferred to the ResNet backbone. The feature map subsequently goes through a FC layer, now with basic zoomed LC features. By integrating all of the zoomed and initial features, the final FC layer produces the class prediction. The dashed connectors and outputs are optimized during training and can output as needed during inference. For the PS component, input  $N$  PS ( $x(f)$ ) and images are computed directly from the LCs, with the process mirroring that of the LC component. After feature extraction with ResNet, these features are used as RPN input. The RPN structure uses the FPN (thick rectangular box region), incorporating additional information from the original image. Next, fold the raw LC according to the most significant frequency in the chosen PS region. The folded LC and basic frequency and folding features are collectively sent to the FC layer for classification. Lastly, the parameter component processes the preset parameters with a FC layer.

**Table 2.** Training Performance on Validation Set

Model Component	Accuracy
LC Component	$0.866 \pm 0.008$
PS Component	$0.931 \pm 0.006$

**Table 3.** Hyper-parameters

Hyper-parameter	Value
Batch size	96
Learning rate	$5 \times 10^{-4}$
Weight decay	0
Number of proposal regions	6
Number of classification regions	4
Input image size	(256, 512)
Zoomed LC image size of LC component	(256, 512)
Zoomed phase image size of PS component	(224, 224)

model accuracy, which is the proportion of instances that are correctly classified. Though we implement the parameter component, we do not train it because we want to compare our model with other works that rely solely on LC. All models are trained for more than 100 epochs until a significant decrease in the accuracy of the validation set was observed. A learning rate reduction schedule is implemented at the 60-th and 100-th epochs, with each reduction being by 50%. The maximum number of epochs allowed is set to 500. Various learning rate schedules are tested, but no significant differences are observed. We also enable automatic mixed precision in our training process to save memory and increase efficiency.

The best average training performance with cross validation for LC and PS components are shown in Table 2. Based on this model, Table 3 lists the hyper-parameters selected for this work. We generate proposal regions during the training phase and calculate their losses. However, for the output, only the features of top-N proposal regions (N is the number of classification regions) are used. In our experiment, the number of proposed regions and the number of classification regions do not have a significant impact on the PS component, but they are more sensitive in the LC component. We chose this value not only based on performance, but also to make it easier to combine these two components by selecting the same number of regions.

Our LC component and PS component can be merged by incorporating a FC layer to fuse their features. Our package includes a parameter component, but for the sake of fair comparison with previous studies, we did not enable it in this experiment. There are two possible approaches for training this combined model. First, the LC and PS components can be trained separately, after which their parameters are fixed, leaving only the final FC layer free for fusion. Alternatively, and this is our preferred method, the combined model can be trained from scratch. While the first approach tends to be simpler and quicker, the latter method generally delivers better performance.

#### 4.1. Model Evaluation

With fixed hyper-parameters, we retrain the model on the whole training dataset and evaluate it on the test dataset. The performance on the test dataset is listed on Table 4 for both variable star dataset and combined dataset. The accuracy is the ratio of the number of correctly classified labels and the ground truth number. Precision, Recall and

**Table 4.** Performances on Test Set

Model Component	Dataset	Accuracy	Precision	Recall	$F_1$ score
LC Component	Variables (Kepler, TESS)	0.887	0.910	0.891	0.900
	Variables + Transients (Kepler, TESS, ZTF)	0.822	0.725	0.700	0.705
PS Component	Variables (Kepler, TESS)	0.934	0.954	0.932	0.941
	Variables + Transients (Kepler, TESS, ZTF)	0.845	0.732	0.708	0.715
Combined	Variables (Kepler, TESS)	0.942	0.957	0.946	0.952
	Variables + Transients (Kepler, TESS, ZTF)	0.870	0.762	0.779	0.757

NOTE—Precision, Recall, and  $F_1$  score are calculated with macro-averaged.

$F_1$  score are calculated in a macro-average way:

$$\text{Precision} = \frac{\text{TP}}{\text{TP} + \text{FP}}, \text{Recall} = \frac{\text{TP}}{\text{TP} + \text{FN}}, F_1 = 2 \frac{\text{Precision} \times \text{Recall}}{\text{Precision} + \text{Recall}},$$

where TP, FP, and FN are true positive, false positive, and false negative. Generally, our models demonstrate comparable performance across all these metrics, similar to [Audenaert et al. \(2021\)](#) for variables, and [Sánchez-Sáez et al. \(2021\)](#) for the combined dataset. However, because we mixed their datasets to train a more general model, our dataset is not as homogeneous as theirs. Therefore, we need to perform separate analyses for different classes of data, which requires calculating confusion matrices.

The confusion matrices for the variable star dataset are presented in Figure 4 separately for the LC and PS components, and in Figure 5 for the combined model that integrates both LC and PS components. Based on the results presented in Table 4 and Figure 4, it is evident that the PS component can outperform the LC component, and the combined model returns a better performance than any individual component. This observation aligns with the inherent characteristics of variables. Compare with T'DA results ([Audenaert et al. 2021](#)), the accuracy is comparable, but the confusion matrix shows our  $\gamma$  Dor/SPB stars are mainly misclassified with Rot/CEB. This confusion is also somewhat evident in [Audenaert et al. \(2021\)](#) because they are sharing a similar parameter space on frequency and variability. However, our relatively weaker performance is mainly attributed to the TESS samples. The shorter baseline of TESS makes g-mode pulsations not as clear as in the Kepler sample in the frequency domain. This confusion can be greatly reduced by introducing stellar physical parameters.

Figure 6 and Figure 7 illustrate the confusion matrices of our models of combined dataset. As we expected, most transients are more accurately classified in the LC component than in the PS component. This is because their non-periodic features are more clear in the time domain. Our models outperform AleRCE ZTF classification ([Sánchez-Sáez et al. 2021](#)) in some classes, particularly CV/Novae and YSOs. This is due to our direct use of LC morphology information in the LC component, as evidenced by comparison with the PS component. However, our models underperform when it comes to transients, especially SN Ibc which is nearly always misidentified as SN Ia. As explained in [Sánchez-Sáez et al. \(2021\)](#), this confusion may be intrinsic because the physical mechanisms that cause variability are similar ([Arnett 2008](#)) and cannot be easily distinguished from LC shapes alone. Therefore, more specialized models and metrics are necessary for SN classification.

To investigate the impact of zooming ability on performance, we conducted a simple ablation experiment. Specifically, we disabled the zooming modules and computed the accuracy of our trained LC component for variable star modeling using only raw LC data. The resulting accuracy is 0.749, which is significantly lower than the 0.887 achieved with zooming enabled (see Table 4). This suggests that our LC model benefits greatly from zooming functionality. We also applied this experiment to the PS component and found little improvement in accuracy due to most frequency information being captured by overall PS. However, this does not imply that zooming is unnecessary for PS component, because it is crucial for model robustness and detecting peculiar targets.

An important feature of our model is its ability to not only predict class labels, but also provide intermediate results for monitoring the model's performance and conducting further analysis. To intuitively see the intermediate results of our model, Figure 8–13 are examples of displaying our classification intermediate results. These figures demonstrate

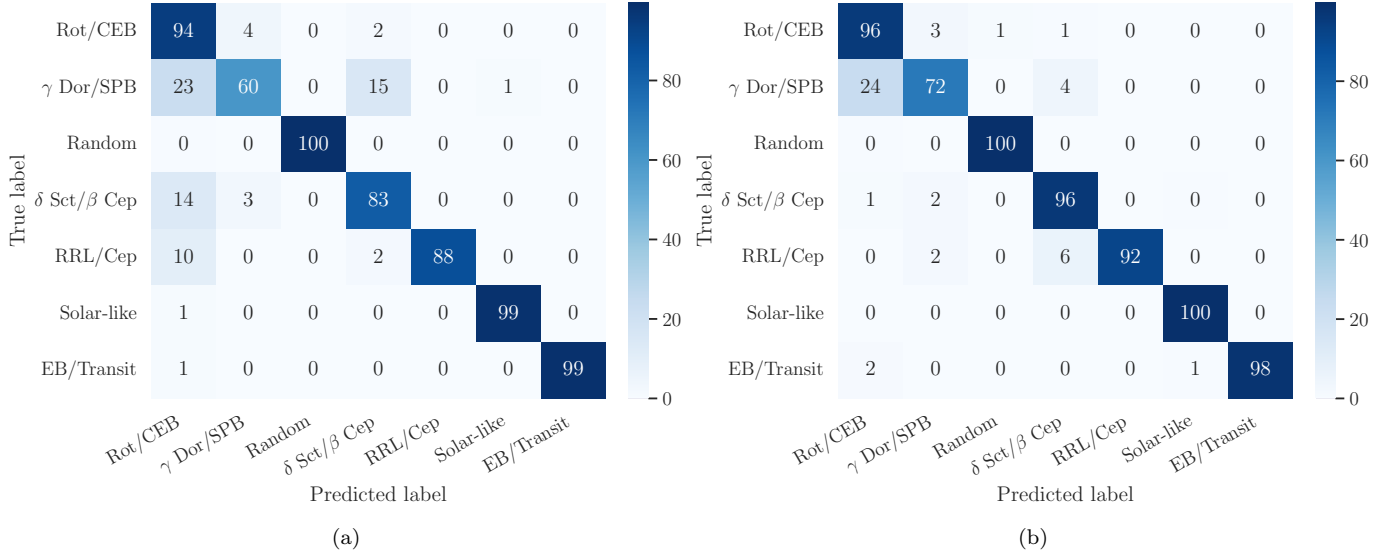


**Figure 4.** Normalized confusion matrix of the best LC component (a) and PS component (b) model on the variable test set. The numbers presented in the matrix represent the proportion of objects that are correctly identified as positive for a specific class (column) out of the total number of objects belonging to that class (row).

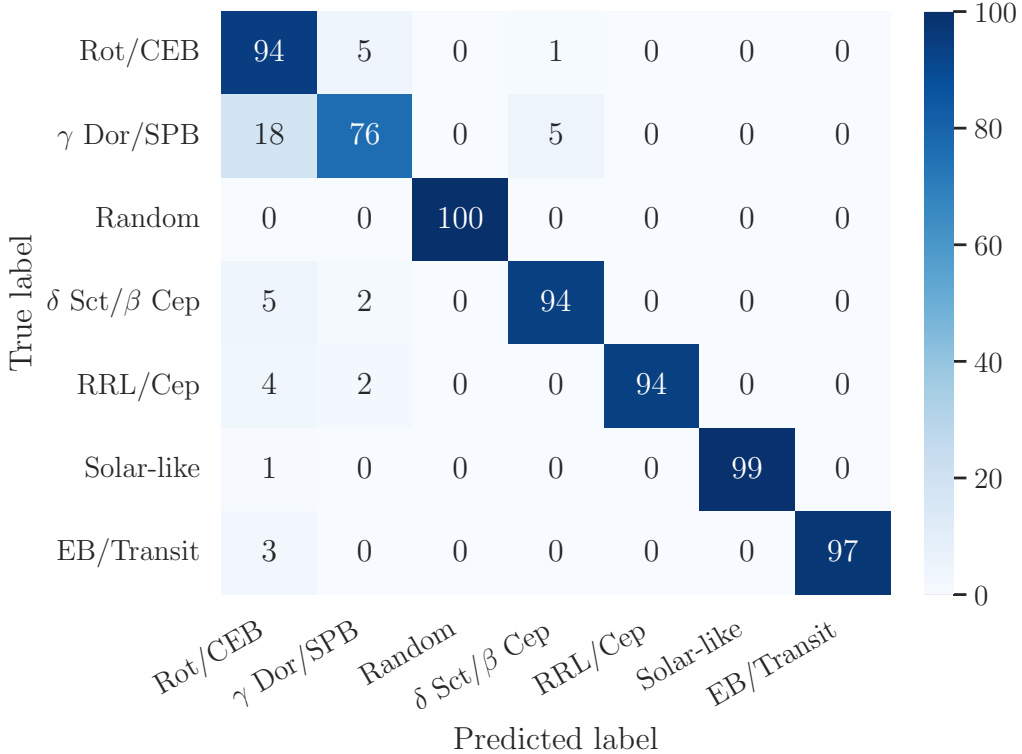


**Figure 5.** Normalized confusion matrix of the best combined model on variable test set. Similar to Figure 4.

the model's selection of zooming regions and its classification predictions for each region. As shown in Figure 9, 8, and 11, our LC component model is capable of accommodating significant gaps in observations by automatically adjusting the zooming windows to focus on different regions. For the observation with only a few points (Figure 10),

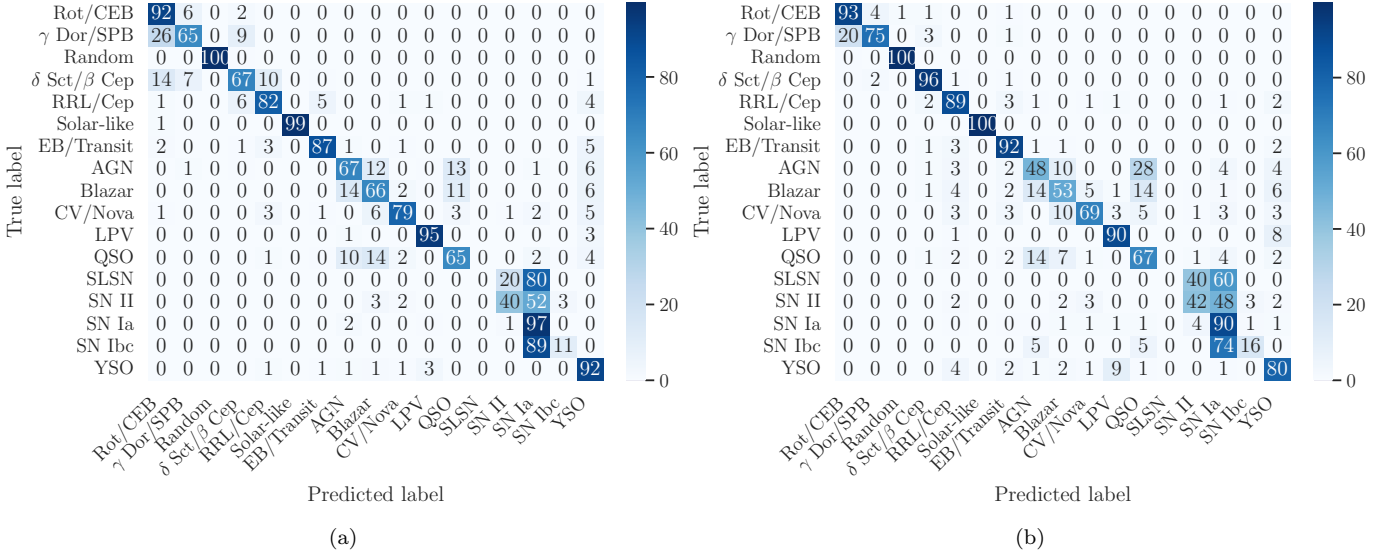


**Figure 6.** Normalized confusion matrix of the best LC component (a) and PS component (b) model on the combined test set. Similar to Figure 4.

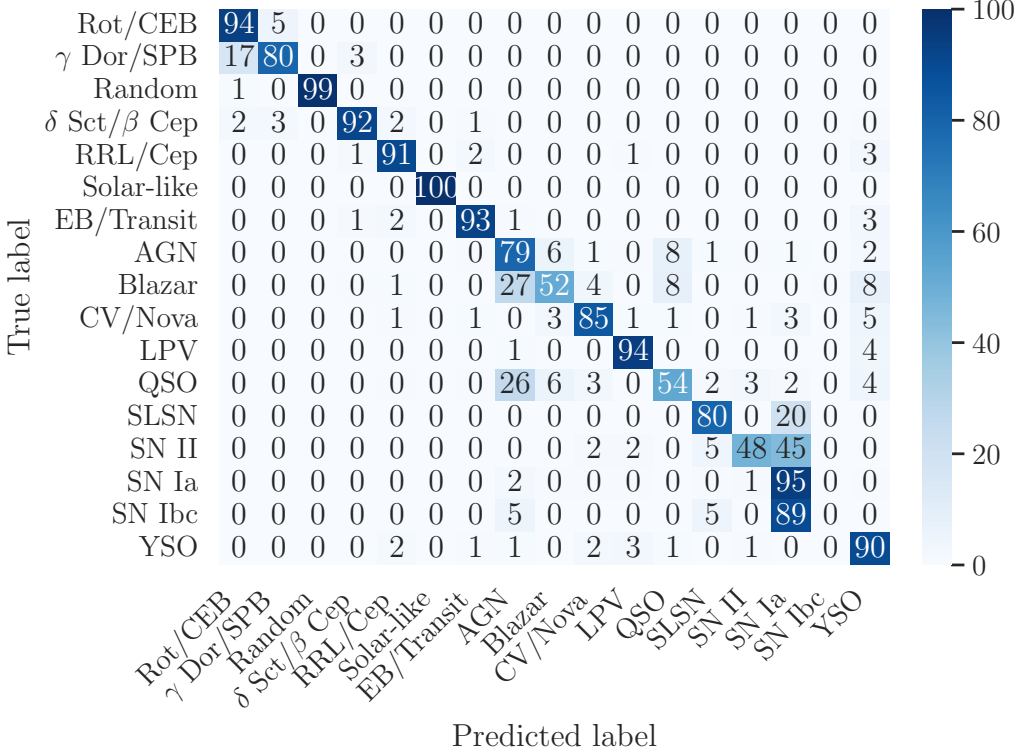


**Figure 7.** Normalized confusion matrix of the best combined model on combined test dataset. Similar to Figure 4.

LC component stops zooming automatically. In many cases, different zoomed regions can output different predictions, but the integrated prediction is usually more reliable.

Since our model is trained on both space- and ground-based data with adapting to different time scales and observational cadences, we can test if it can be general for different missions. Here we choose the All-Sky Automated Survey for SuperNovae (ASAS-SN) g-band LCs from the most recent variable catalog (Shappee et al. 2014; Christy

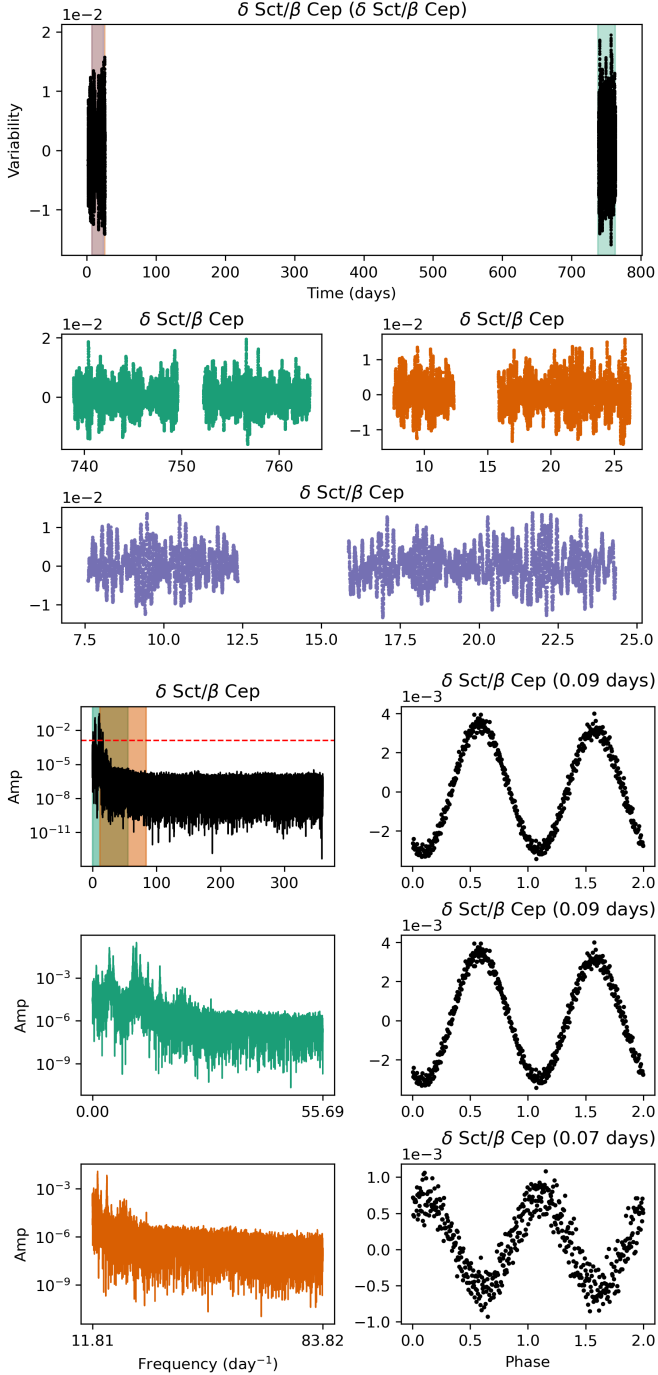


**Figure 8.** Classification intermediate results of TIC 397330244, which is a  $\delta$  Scuti star. From top to bottom, the first panel is the raw LC with three zoomed regions covered by semi-transparent colors. The second and third rows are zoomed LCs plotted with same colors with the zoomed regions in the first panel. The predictive labels are displayed in the titles of each panel. The title of the top panel indicates the label derived from the entire LC component, and solely from the raw LC, which is specified in the brackets. After the LC component, PS component starts from the fourth row, the left panel is the PS with zoomed regions, and the dashed red line is the false alarm level at 1% probability. The right panel shows the corresponding folded LC with adopting the most significant peak of the left PS. The bottom two rows follow the same rule. The predictive labels are also displayed in the titles of each right panel of PS component, the title of left top panel of PS component is derived from the entire PS component.

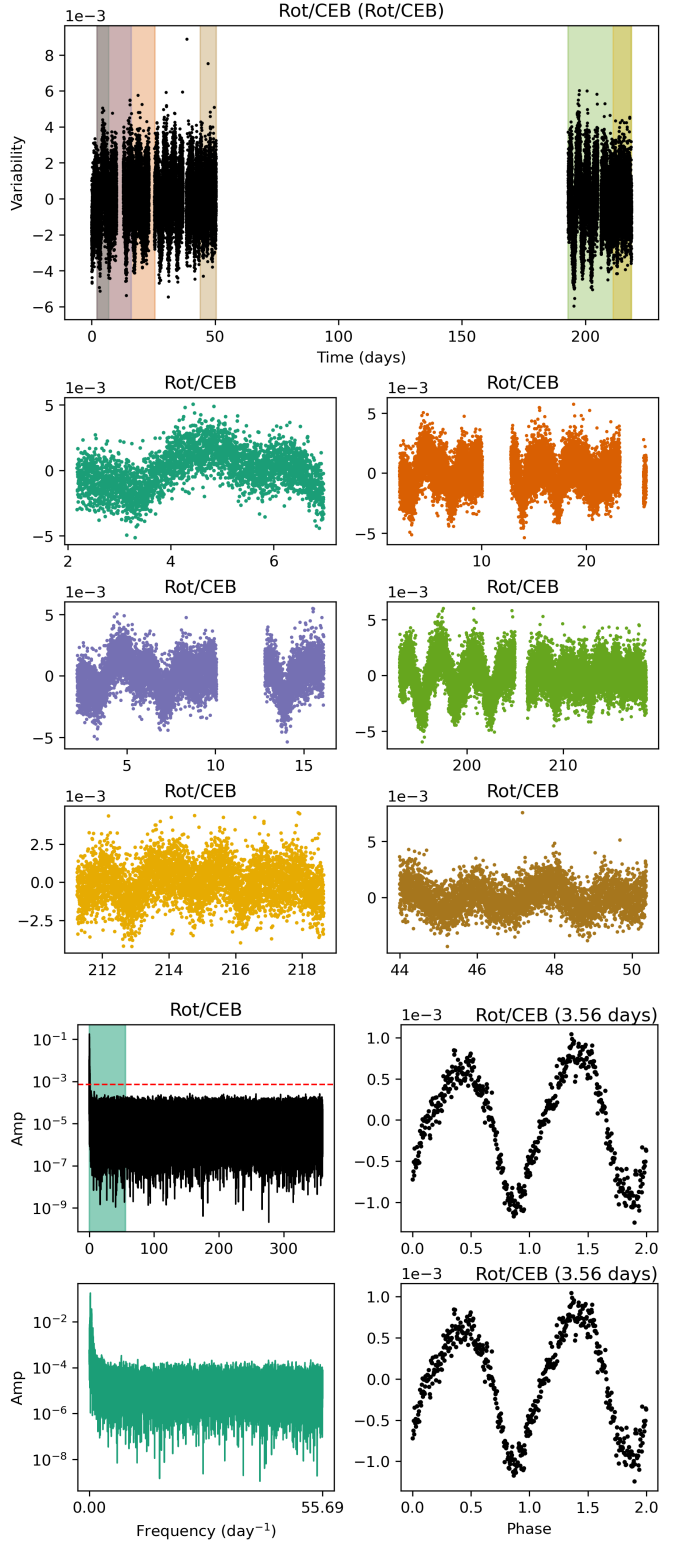


**Figure 9.** Classification intermediate results of TIC 470109695, which is a rotator. Similar to Figure 8.

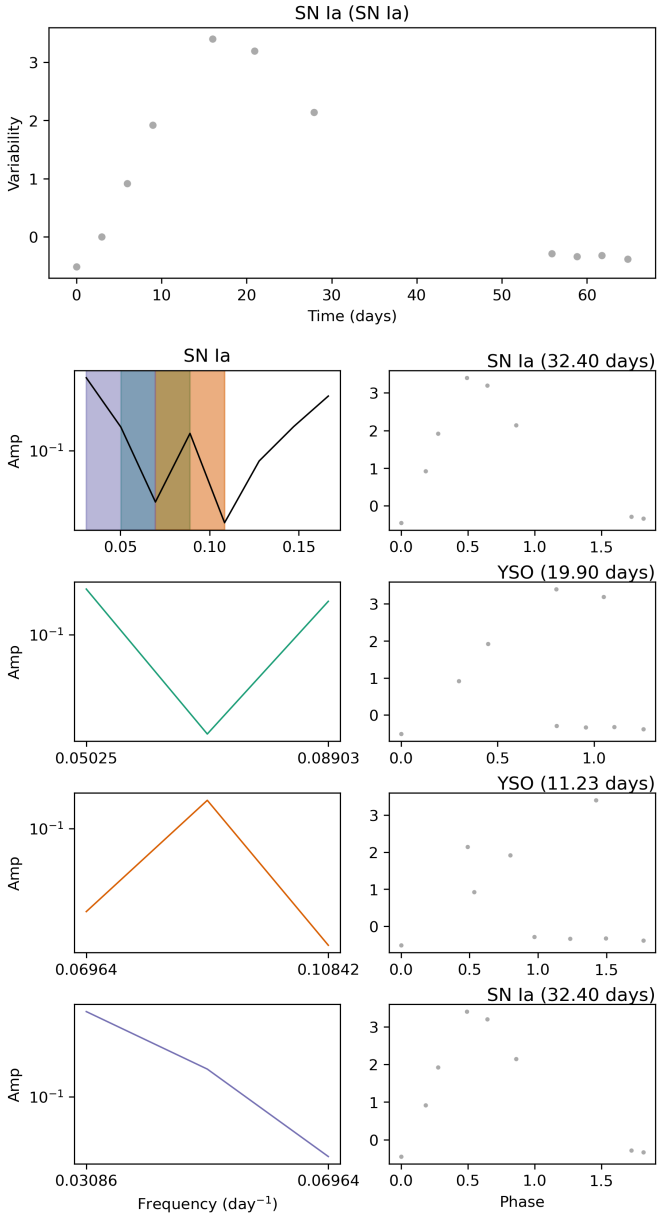


**Figure 10.** Classification intermediate results of ZTF18abuhjv, which is a SN Ia from ZTF alert system. Similar to Figure 8 but plot as gray scale for data from different observational bands.

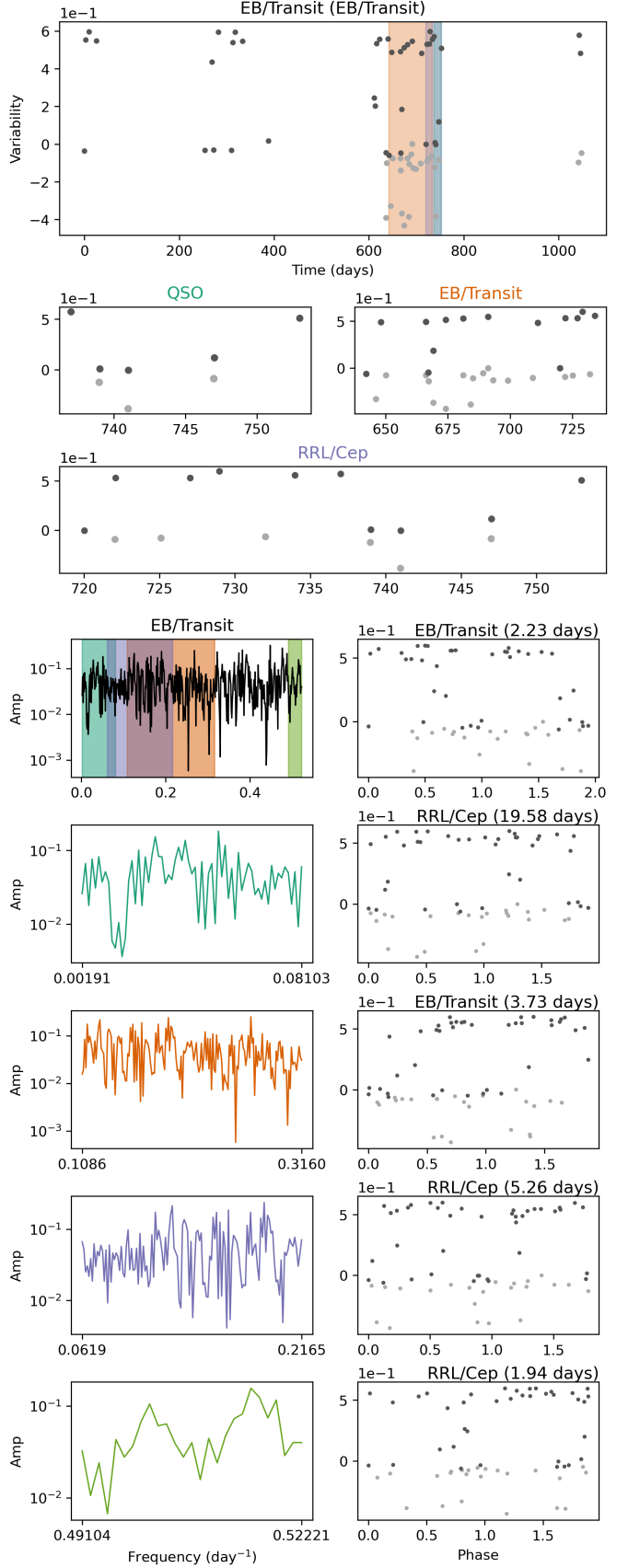


**Figure 11.** Classification intermediate results of ZTF19aapkqyk, which is an EB from ZTF alert system. Similar to Figure 10.

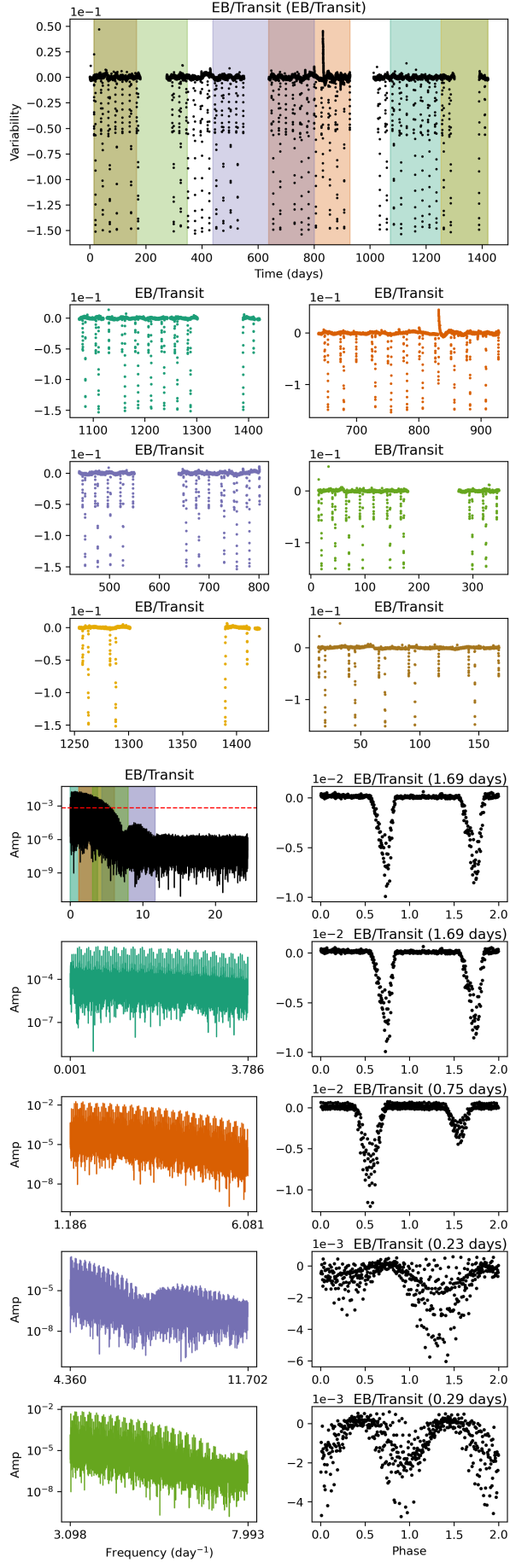


**Figure 12.** Classification intermediate results of KIC 10651945, which is an EB. Similar to Figure 8.

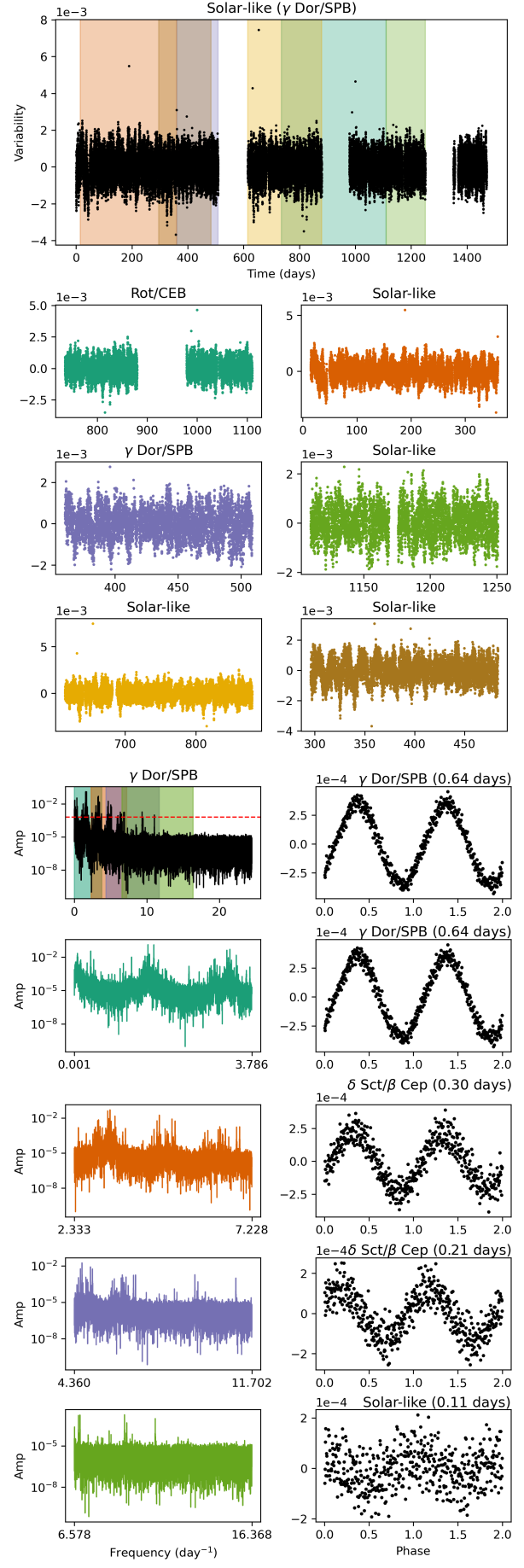


**Figure 13.** Classification intermediate results of KIC 10091792, which is a  $\gamma$  Dor. Similar to Figure 8.

et al. 2023). Because ASAS-SN taxonomy is different from ours, we select some common classes and sampling objects with top-100 probabilities for each class. This procedure is to make sure the results are more reliable. Without any fine-tuning and preprocessing on the ASAS-SN LCs, we treat them as single band LCs and directly send them to our model (trained on combined dataset). For ASAS-SN EB, our model reaches to 81% accuracy; for  $\delta$  Scuti, we get 37% accuracy; for RRL, we can get 94% accuracy. Our model performs with satisfactory accuracy on EB and RRL for their prominent features, but quite low on  $\delta$  Scuti stars. Figure 14 displays a correctly classified EB and Figure 15 shows a misclassified  $\delta$  Scuti star. When comparing with the accurately classified TESS  $\delta$  Scuti stars (Figure 8), it is observed that without physical parameters, a decrease in photometric precision can lead to misclassification of  $\delta$  Scuti stars as RRL due to their distorted shape. However, the PS component in Figure 15 provides the correct label and indicates an uncertain prediction, which can be utilized in Section 4.2.

Dealing with lower photometric precision LCs requires a model that accounts for the uncertainty in the observation, which is not currently included in our model. While we do consider photometric uncertainties when calculating multi-band Lomb-Scargle, other physical quantities and region selection are calculated without accounting for uncertainty. As a result, the performance of our model may decrease when the photometric precision is lower than ZTF. To address this issue, more complex data preprocessing or model fitting operations may be required in the future model (see Section 6).

#### 4.2. Model Uncertainty

Estimating predictive uncertainty for a machine learning model in a reliable manner is essential for decision making and model interpretability. However, most classical machine learning models and modern deep learning models are observed to have a miscalibration in their confidence (Niculescu-Mizil & Caruana 2005; Guo et al. 2017).

To address this issue, we calculate the calibration error of our model with the expected calibration error (ECE; Naeini et al. 2015) and maximum calibration error (MCE; Naeini et al. 2015). ECE is the expectation of difference between confidence and accuracy, which can be estimated as

$$\text{ECE} = \sum_i^{N} b_i |p_i - c_i|, \quad (3)$$

$$\text{MCE} = \max_i (p_i - c_i), \quad (4)$$

where  $N$  is number of bins, for each bin  $i$ ,  $p_i$  is the prediction accuracy, and  $c_i$  is the average confidence score.  $b_i$  is the fraction of data points in bin  $i$ . An ideal calibrated classifier would have both the ECE and MCE equal to 0. In this study, we selected a commonly used value of  $N = 15$  and obtained the ECE of 0.082 and the MCE of 0.391 for our optimal combined model trained on the combined dataset. These results are consistent with previous studies conducted on various CNN models (ECE 4–16%, MCE 20–40% Guo et al. 2017), indicating common miscalibration. Figure 16 shows the corresponding reliability diagram, which is the expected sample accuracy as a function of confidence (Guo et al. 2017), and the deviation from the diagonal line indicates imperfect calibration.

In order to quantify the uncertainty of our deep learning classifier and make our model more applicable for decision making, we employ a technique based on conformal prediction (Vovk et al. 1999), a framework that can produce prediction sets with provable coverage guarantees. It guarantees that the prediction sets are designed to contain the true label of a new test instance with a high probability, regardless of the underlying data distribution or model assumptions. Specifically, we adopt the regularized adaptive prediction sets (RAPS; Angelopoulos et al. 2022) as our final predictive sets.

To calibrate our model, we have to make a calibration dataset, so we split our test dataset to a calibration dataset and a validation dataset with equal sizes. After the calibration on our best performance model with RAPS at the 5% significant level, we show the calibration performance in Table 5, where the accuracy is calculated on the split validation dataset. Because the validation data are from the test dataset, the Top-1 accuracy is very similar to the results in Table 4. The predictive set coverage is closer to 95%, consistent with the pre-specified 5% confidence level. The average size of prediction sets are also listed in Table 5.

After conformal calibration, our model become more applicable for unseen samples. For instance, when we test our conformal calibrated model to ASAS-SN  $\delta$  Sct objects as discussed in Section 4, the 95% coverage predictive sets returned an accuracy of 79%, which is significantly better than the point prediction. However, the average size of these prediction sets is 3.99, which is larger than our calibrated average value. This excessive length of the prediction

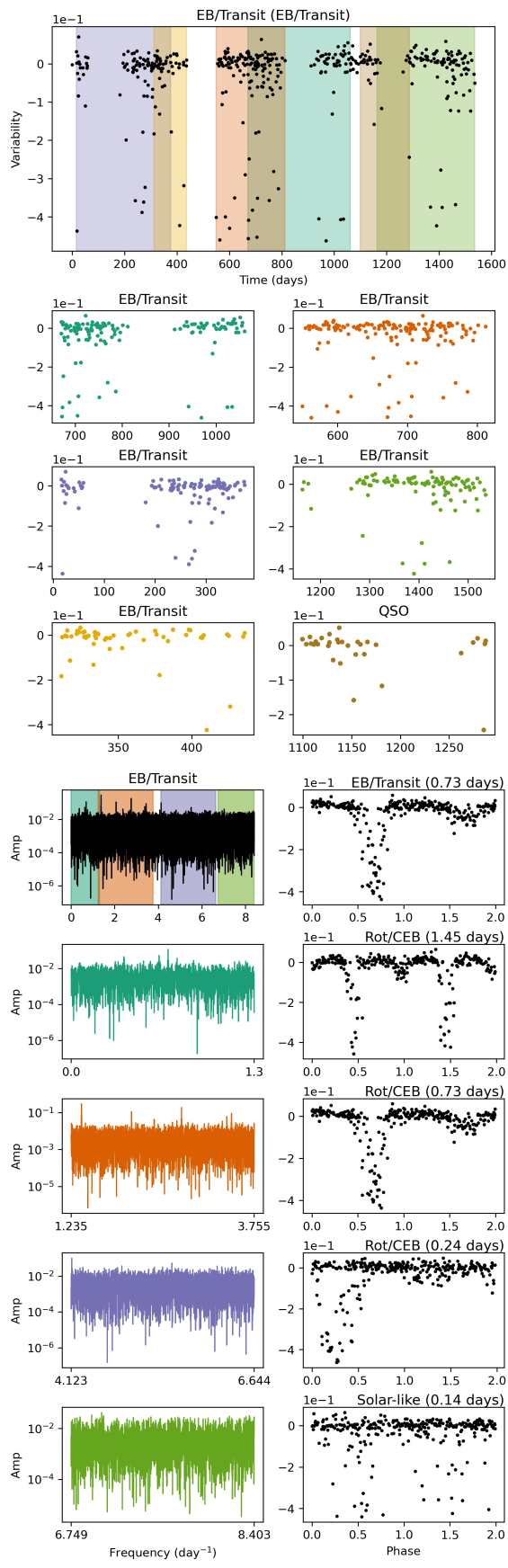


**Figure 14.** Classification intermediate results of ASASSN-V J202436.43+133428.1, which is an EB system with correctly classified in our model. Similar to Figure 8.

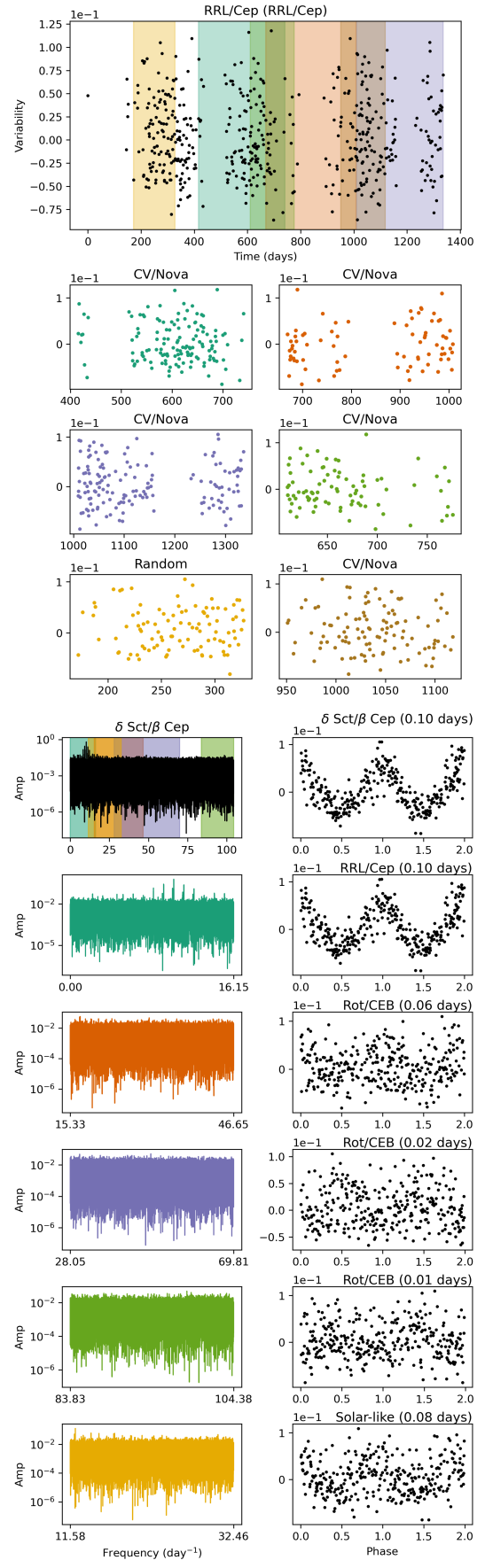


**Figure 15.** Classification intermediate results of ASAS-SN J082703.44-265001.6, which is a delta scuti object but misclassified by our model. 95% conformal predictive set is [RRL/Cep,  $\delta$  Sct/ $\beta$  Cep, Rot/CEB, EB/Transit]. Similar to Figure 8.

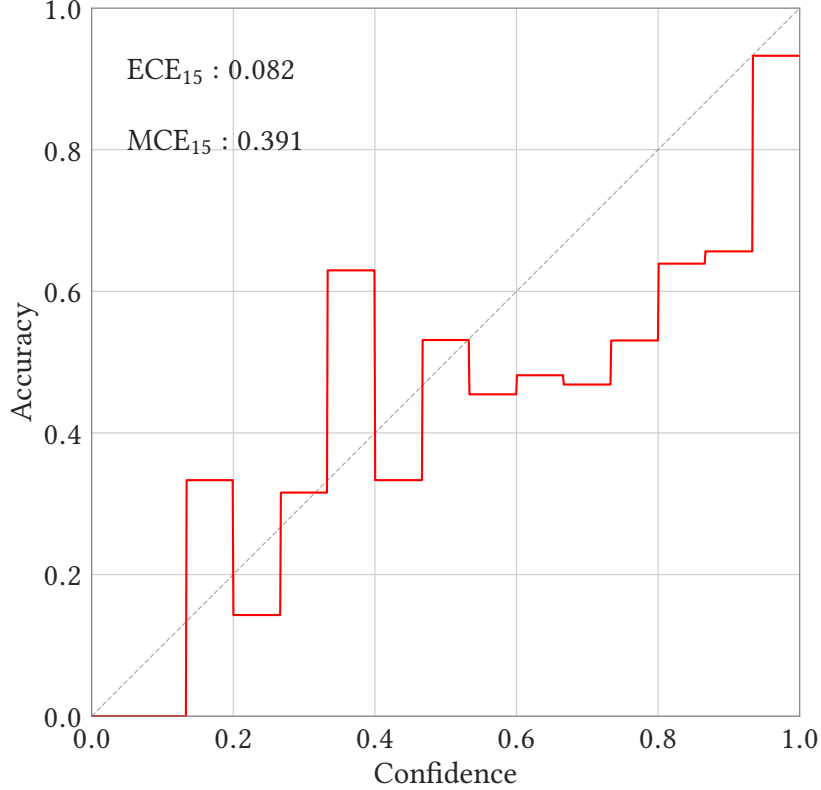


**Figure 16.** Reliability diagram of our sample

**Table 5.** Conformal calibration results with 95% coverage rate

Model Component	Dataset	Accuracy		Coverage	Size
		Top-1	Top-5		
Combined	Variables (Kepler, TESS)	0.934	0.999	0.935	1.11
	Variables + Transients (Kepler, TESS, ZTF)	0.877	0.991	0.953	1.79

sets reflects the model’s uncertainty and may serve as an indicator for anomalous targets. We will further elaborate on this in Section 5.

## 5. PECULIAR OBJECTS DETECTION

The goal of typical classification algorithms is to achieve accurate and unambiguous predictions. However, in practice, there are often objects that are difficult to classify or that do not fit into any known category. These objects may be known types but are not included in the training dataset, or they could be something currently unknown. This issue is crucial yet difficult and is generally referred to as out-of-distribution (OOD) or out-of-sample detection. Related problems such as anomaly detection, novelty detection, and outlier detection are the same in essence but with varying degrees of unseen samples.

Once a model is able to distinguish whether a sample comes from in-distribution (ID) or OOD, it can be more general and reliable for practical astronomical observations. In addition to classification, it may also provide direct assistance in the search for unknown peculiar targets. In recent astronomical observations, there has been a notable increase in detecting LC anomalies due to the growing demand for the identification of uncommon transients (e.g., Prughinskaya et al. 2019; Malanchev et al. 2021; Villar et al. 2021), where they applied an isolation forest algorithm in the context of active learning. Inspired by KIC 8462852 (Boyajian’s star; Boyajian et al. 2016), some more general LC anomaly detection has also been performed on Kepler data (Giles & Walkowicz 2020; Martínez-Galarza et al. 2021). However, their anomalies are detected mainly based on the clustering of features from the data. Instead of using the

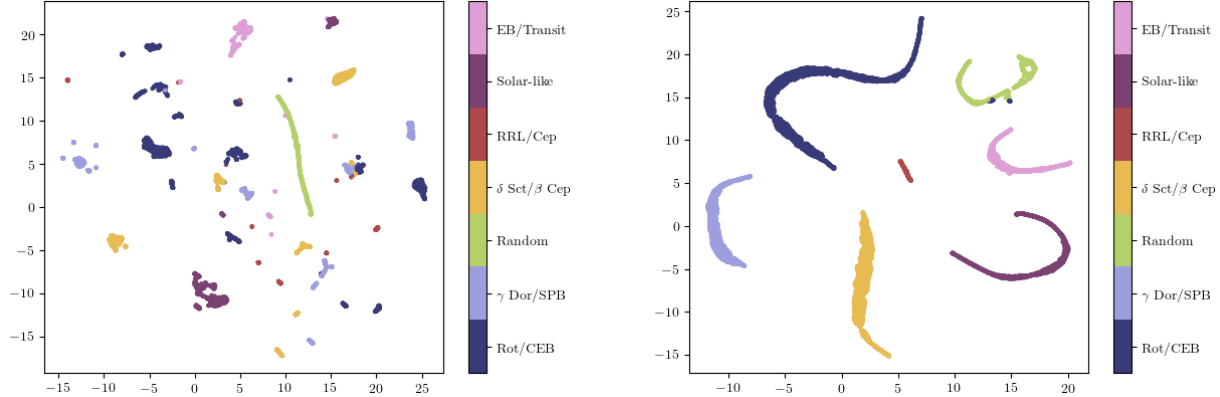


**Figure 17.** UMAP of LC component’s feature layer (left figure) and PS component’s feature layer (right figure) trained on the variables dataset.

raw features from the data, since we already have a well performed classifier, we can abstract classification features along more physically meaningful directions to apply OOD detection. To do so, we apply a few different approaches at different levels.

Traditionally, unsupervised dimensionality reduction techniques algorithms such as t-SNE (van der Maaten & Hinton 2008) and uniform manifold approximation and projection (UMAP; McInnes et al. 2020) are often used for outlier detection. Figure 17 displays the UMAP of the penultimate feature layer, i.e., the layer before the FC layer. For the LC component trained on a dataset consisting of variables. It shows some distinct groups corresponding to our predefined classes. Compare with the UMAP of PS component (left sub-figure of Figure 17), the LC component’s features show multiple clusters at different locations, indicating worse performance of OOD detection on LC component. However, these algorithms are primarily designed for visualization and exploration of high-dimensional data, they have some inherent issues such as sensitivity to hyper-parameters, and lack of built-in outlier probability measures may hinder their efficacy. Here we don’t use them for OOD detection but present them as an intuitive visualization of the penultimate features.

Recent progress on OOD detection on image tasks makes full use of the features of neural networks and employs various methods to attempt to obtain OOD results (Yang et al. 2022). We implement some of these methods and apply them in our LC classification framework. At first, to evaluate the performance of those OOD metrics, we have to create an OOD sample. However, creating an OOD sample is difficult because the OOD can be at different levels for different scenarios. In this study, we select heartbeat stars from Kepler (Prša et al. 2011; Abdul-Masih et al. 2016)<sup>8</sup> as the OOD sample.

A lot of OOD metrics are available. For instance, maximum softmax probability (MSP; Hendrycks & Gimpel 2018) is the most straightforward way to distinguish ID and OOD data based on their maximum softmax scores. Out of distribution detector for neural networks (ODIN; Liang et al. 2020) introduces temperature scaling and input preprocessing to make ID data and OOD data have more distinct distributions. Energy score (Liu et al. 2021b) is a modification of logit borrowing the expression of free energy and the partition function. Virtual outlier synthesis (VOS; Du et al. 2022) generates virtual outliers on the penultimate layer based on the multivariate Gaussian distribution conditioned by the classes. Directed Sparsification (DICE; Sun & Li 2022) prunes the less contributed neurons to make the OOD data more separate from ID data. Virtual-logit matching (ViM; Wang et al. 2022) calculates an additional logit representing the virtual OOD class generated from the residual of the feature against the principal space, and then matched with the original logits by a constant scaling. The probability of this virtual logit after softmax is the indicator of OOD-ness.

Among the metrics mentioned above, VOS needs to retrain the model, while DICE requires replacement of the last FC layer, and ViM aligns the projection with logit through the weights and biases from the FC layer. Consequently, we retrain our model, enabling VOS in the process. Following this, we compute the DICE and other metrics, using both the VOS-enabled and VOS-disabled models for comparison. The best OOD detection performance comes from

<sup>8</sup> <http://keplerebs.villanova.edu/>

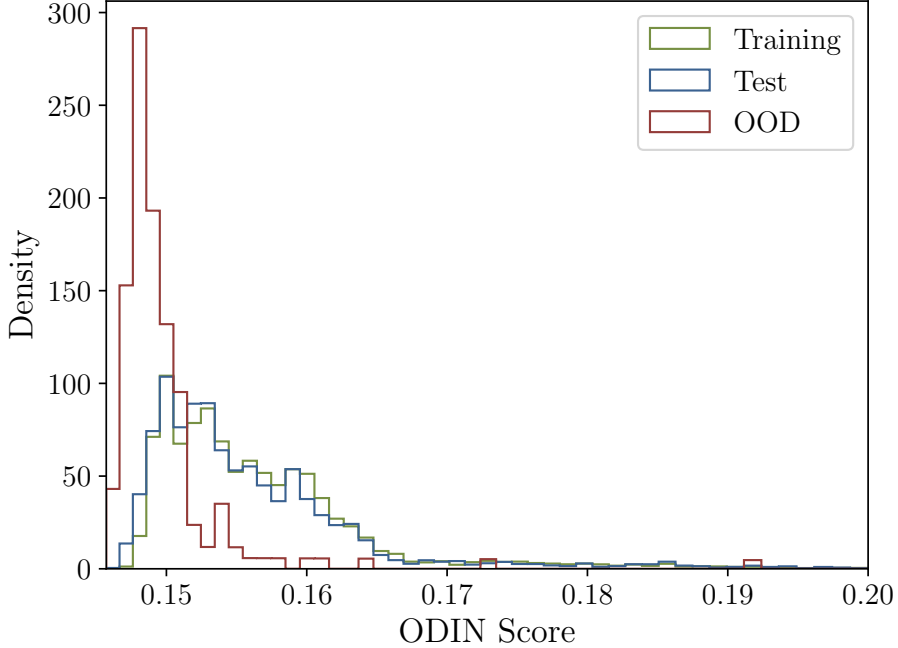


**Figure 18.** OOD ODIN score distribution. The distribution is truncated to ODIN scores lower than 0.2.

the PS component trained on variable stars. Table 6 lists the OOD performances with different OOD metrics. We utilized the area under the receiver operating characteristic (AUROC) and false positive rate at 95% true positive rate (FPR@TPR95) as metrics to evaluate the efficiency of OOD detection. A higher AUROC indicates better ability to distinguish between OOD and ID, while a lower FPR@TPR95 signifies fewer misclassifications of ID samples as OOD when 95% of OOD samples are correctly detected. Figure 18 displays the best ODIN score distributions for training, testing, and OOD datasets. It is evident that training and test samples have identical distributions, but OOD data is located in a lower ODIN score region and can be distinguished from training/test data using a threshold. This threshold can be determined with an ROC curve shown in Figure 19. For a TPR of 95%, the threshold is 0.149; lower TPR values result in higher thresholds. Retraining models from scratch for VOS affects model performance on ID data. In our case, we achieve an accuracy of 0.928 for PS components on variable datasets, a result that is acceptable in most instances.

We also calculated OOD metrics for the LC component and our combined model. For the LC component, the best AUROC is 0.65, which is significantly worse than the PS component. This suggests that either the metrics used are not sensitive enough to detect OOD samples, or as shown on the UMAP plot, the features from the LC component are much more complex than those from the PS component and cannot be easily represented by simple OOD indicators. Our combined models have three FC layers after the penultimate feature layer, thus VOS, DICE, and ViM are not available, the best AUROC is just slightly above 0.5, indicating that the combined model may be suffering the same issue as the LC component and can hardly distinguish the OOD sample with current metrics.

Detecting OOD is a challenging task. The reason machine learning classifiers can fail in real-world tasks is because of the discrepancies between training and testing distributions. These classifiers frequently yield high-confidence predictions that are, unfortunately, incorrect. If the model does not have the capability to flag potential errors, its adoption could be restricted, or it could even lead to severe accidents. A well-calibrated model can be helpful when encountering OOD sample. As we discussed in Section 4.2, our conformal calibrated model can return a predictive set with guaranteed coverage at a specific probability, the predictive sets give a hint to return the OOD objects. For example, we applied our conformal calibrated model to the known Kepler oscillating EB sample(Gaulme & Guzik

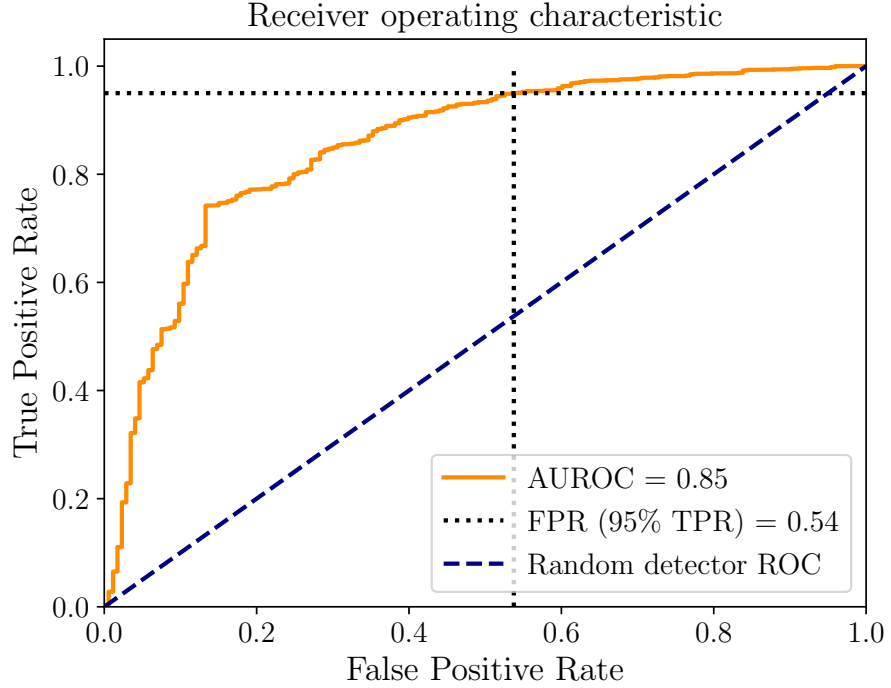


**Figure 19.** OOD ODIN ROC curve

**Table 6.** OOD performances of PS component

OOD Detection Algorithms		AUROC $\uparrow$	FPR@TPR95 $\downarrow$
With DICE	MSP	0.80	0.88
	ODIN	0.80	0.89
	Energy	0.84	0.71
	ViM	0.73	0.90
With VOS	MSP	0.76	0.77
	ODIN	<b>0.85</b>	<b>0.54</b>
	Energy	0.53	1.00
	ViM	0.60	0.94
Without DICE	MSP	0.69	0.88
	ODIN	0.72	0.81
	Energy	0.63	0.98
	ViM	0.83	0.63
Without VOS	MSP	0.67	0.94
	ODIN	0.68	0.94
	Energy	0.70	0.95
	ViM	0.80	0.79

2019), obtaining an accuracy of 0.896. For the correctly classified objects, 47.6% among them have predictive sets with multiple candidates, indicating possible pulsating components.

## 6. DISCUSSION

While our model is general for different time lengths and cadences, it does have its limitations. For instance, it cannot effectively handle extremely short cadence data such as gravitational waves, which possess a sampling rate of 16 kHz. Processing this type of data in the time domain is wholly unsuitable. Furthermore, extremely short cadences may exceed our frequency calculation range. As the frequency increases, so does the computation time, and this could be problematic. Lengthy time series like combining two independent missions together with a large observation gap is possible in our model, but unless the characteristics are notably distinguishable, the model's zooming ability may fail. Potential solutions can include increasing the image size or iteratively applying the model to the selected regions. Currently, our model only supports two colors. Additional colors can be seamlessly implemented as different gray scales or appended as new image channels. If the input requires many colors (more than 20), the development of new methods may be required. However, this might not be necessary for classification. Moreover, the impact of systematics on our model can be substantial, affecting both the time and frequency domains. As systematics are influenced by the unique characteristics of different surveys, there is no universal solution for them. Our current model is trained using preprocessed data, specifically the PDCSAP from Kepler/TESS and corrected ZTF LCs. Therefore, the input LC for our model must be at least corrected for systematic signals.

Beyond normal optical LC, our model can be applied on general time series classifications, such as other wavelengths like radio, X-ray, or any narrow bands long term observations are also applicable. However, for these specific cases, the model would require retraining from scratch. In this work, we deliberately limit our dataset to facilitate comparison with previous performances; more completed dataset from various sources are ready for practical usage. Our classification framework will be expanded to include more detailed categories. By utilizing the parameter component, we can optimize our model using lots of established missions, ongoing surveys such as the Tianyu Project (Feng et al. in preparation) and Sitian Project (Liu et al. 2021a), and simulated dataset from the Vera Rubin Observatory's PLAsTiCC project (Kessler et al. 2019). Additionally, since our model can be applied to most photometric systems, our classifier provides a model that can be directly used or easily fine-tuned for various small-scale observation projects. We have made all of our models available <sup>9</sup>, users can choose different models based on their specific needs.

Current large language models demonstrate superior proficiency in understanding natural language. It can replace or extend our parameter component while accepting our intermediate data along with some incomplete and unstructured data (e.g., instrumental specific systematics diagnostics, external environment information, literature conclusions). Future possible advanced machine learning models with multi-modal capabilities may have the ability to reason and imagine at a human level. These networks can autonomously assess the completeness of information and seek additional data, including experimental manipulation of raw data (e.g., fitting data with model and adjust parameters for comparison). This could lead to highly reliable and interpretable classification and analysis models in the future.

<sup>1</sup> We would like to express our gratitude to Masataka Aizawa for his valuable suggestions and to Shuai Zha and Zhenyu  
<sup>2</sup> Zhu for generously providing computing resources. We would also like to extend our thanks to L. A. Balona for  
<sup>3</sup> supplying his complete catalog. We acknowledge the support from the B-type Strategic Priority Program of the Chinese  
<sup>4</sup> Academy of Sciences, Grant No. XDB41000000, and China Postdoctoral Science Foundation (No. 2022M712083). The  
<sup>5</sup> collaboration of this work is supported by the SJTU Global Strategic Partnership Fund (2022 SJTU-Warwick). This  
<sup>6</sup> work is also partly supported by Shanghai Jiao Tong University 2030 Initiative. The authors acknowledge the Siyuan-1  
<sup>7</sup> cluster supported by the Center for High Performance Computing at Shanghai Jiao Tong University, and the Tsung-  
<sup>8</sup> Dao Lee Institute AstroCluster for providing GPU resources that have contributed to the research results reported  
<sup>9</sup> within this paper. Part of the languages have been polished with the assistance of Microsoft Azure OpenAI Service  
<sup>10</sup> (Microsoft Corporation 2023), utilizing both the OpenAI GPT-3.5-0301 (Ouyang et al. 2022) and GPT-4-0613 (OpenAI  
<sup>11</sup> 2023) models.

*Facilities:* Kepler, TESS, ZTF

*Software:* Astropy (The Astropy Collaboration et al. 2013, 2018), Numpy (Harris et al. 2020), PyTorch (Paszke et al. 2019), Matplotlib (Hunter 2007), Jupyter Notebook (Kluyver et al. 2016), Lightkurve (Lightkurve Collaboration

<sup>9</sup> <https://zenodo.org/records/10081600>

et al. 2018; Barentsen et al. 2021), Lightkurve-ext (Cui 2022), Microsoft Azure OpenAI Service (Microsoft Corporation 2023)

## REFERENCES

Abdul-Masih, M., Prša, A., Conroy, K., et al. 2016, The Astronomical Journal, 151, 101, doi: [10.3847/0004-6256/151/4/101](https://doi.org/10.3847/0004-6256/151/4/101)

Allam Jr., T., & McEwen, J. D. 2023, Paying Attention to Astronomical Transients: Introducing the Time-series Transformer for Photometric Classification, arXiv, doi: [10.48550/arXiv.2105.06178](https://doi.org/10.48550/arXiv.2105.06178)

Angelopoulos, A., Bates, S., Malik, J., & Jordan, M. I. 2022, Uncertainty Sets for Image Classifiers Using Conformal Prediction, arXiv, doi: [10.48550/arXiv.2009.14193](https://doi.org/10.48550/arXiv.2009.14193)

Armstrong, D. J., Kirk, J., Lam, K. W. F., et al. 2015, Astronomy & Astrophysics, 579, A19, doi: [10.1051/0004-6361/201525889](https://doi.org/10.1051/0004-6361/201525889)

—. 2016, Monthly Notices of the Royal Astronomical Society, 456, 2260, doi: [10.1093/mnras/stv2836](https://doi.org/10.1093/mnras/stv2836)

Arnett, D. 2008, AIP Conference Proceedings, 1053, 237, doi: [10.1063/1.3009489](https://doi.org/10.1063/1.3009489)

Audenaert, J., Kuszlewicz, J. S., Handberg, R., et al. 2021, The Astronomical Journal, 162, 209, doi: [10.3847/1538-3881/ac166a](https://doi.org/10.3847/1538-3881/ac166a)

Balona, L. A. 2022, Identification and Classification of TESS Variable Stars, arXiv, doi: [10.48550/arXiv.2212.10776](https://doi.org/10.48550/arXiv.2212.10776)

Balona, L. A., & Dziembowski, W. A. 2011, Monthly Notices of the Royal Astronomical Society, 417, 591, doi: [10.1111/j.1365-2966.2011.19301.x](https://doi.org/10.1111/j.1365-2966.2011.19301.x)

Barentsen, G., Hedges, C., Vinícius, Z., et al. 2021, Lightkurve/Lightkurve: Lightkurve v2.0.5, Zenodo, doi: [10.5281/zenodo.4603214](https://doi.org/10.5281/zenodo.4603214)

Becker, I., Pichara, K., Catelan, M., et al. 2020, Monthly Notices of the Royal Astronomical Society, 493, 2981, doi: [10.1093/mnras/staa350](https://doi.org/10.1093/mnras/staa350)

Bellm, E. 2014, The Zwicky Transient Facility (eprint: arXiv:1410.8185), 27–33, doi: [10.48550/arXiv.1410.8185](https://doi.org/10.48550/arXiv.1410.8185)

Bellm, E. C., Kulkarni, S. R., Graham, M. J., et al. 2018, Publications of the Astronomical Society of the Pacific, 131, 018002, doi: [10.1088/1538-3873/aaecbe](https://doi.org/10.1088/1538-3873/aaecbe)

Borucki, W. J., Koch, D., Basri, G., et al. 2010, Science, 327, 977, doi: [10.1126/science.1185402](https://doi.org/10.1126/science.1185402)

Boyajian, T. S., LaCourse, D. M., Rappaport, S. A., et al. 2016, Monthly Notices of the Royal Astronomical Society, 457, 3988, doi: [10.1093/mnras/stw218](https://doi.org/10.1093/mnras/stw218)

Bresenham, J. E. 1987, IEEE Computer Graphics and Applications, 7, 31, doi: [10.1109/MCG.1987.276986](https://doi.org/10.1109/MCG.1987.276986)

Carrasco-Davis, R., Cabrera-Vives, G., Förster, F., et al. 2019, Publications of the Astronomical Society of the Pacific, 131, 108006, doi: [10.1088/1538-3873/aaef12](https://doi.org/10.1088/1538-3873/aaef12)

Charnock, T., & Moss, A. 2017, The Astrophysical Journal Letters, 837, L28, doi: [10.3847/2041-8213/aa603d](https://doi.org/10.3847/2041-8213/aa603d)

Christy, C. T., Jayasinghe, T., Stanek, K. Z., et al. 2023, Monthly Notices of the Royal Astronomical Society, 519, 5271, doi: [10.1093/mnras/stac3801](https://doi.org/10.1093/mnras/stac3801)

Cui, K. 2022, Lightkurve-Ext. <https://github.com/ckm3/lightkurve-ext/tree/main>

Cui, K., Liu, J., Feng, F., & Liu, J. 2022, The Astronomical Journal, 163, 23, doi: [10.3847/1538-3881/ac3482](https://doi.org/10.3847/1538-3881/ac3482)

Donoso-Oliva, C., Becker, I., Protopapas, P., et al. 2023, Astronomy & Astrophysics, 670, A54, doi: [10.1051/0004-6361/202243928](https://doi.org/10.1051/0004-6361/202243928)

Du, X., Wang, Z., Cai, M., & Li, Y. 2022, VOS: Learning What You Don't Know by Virtual Outlier Synthesis, arXiv, doi: [10.48550/arXiv.2202.01197](https://doi.org/10.48550/arXiv.2202.01197)

Elor, Y., & Averbuch-Elor, H. 2022, To SMOTE, or Not to SMOTE?, doi: [10.48550/arXiv.2201.08528](https://doi.org/10.48550/arXiv.2201.08528)

Förster, F., Cabrera-Vives, G., Castillo-Navarrete, E., et al. 2021, The Astronomical Journal, 161, 242, doi: [10.3847/1538-3881/abe9bc](https://doi.org/10.3847/1538-3881/abe9bc)

Gaia Collaboration, Eyer, L., Rimoldini, L., et al. 2019, Astronomy & Astrophysics, 623, A110, doi: [10.1051/0004-6361/201833304](https://doi.org/10.1051/0004-6361/201833304)

Gao, M., Yu, R., Li, A., Morariu, V. I., & Davis, L. S. 2018, Dynamic Zoom-in Network for Fast Object Detection in Large Images, arXiv, doi: [10.48550/arXiv.1711.05187](https://doi.org/10.48550/arXiv.1711.05187)

García-Jara, G., Protopapas, P., & Estévez, P. A. 2022, The Astrophysical Journal, 935, 23, doi: [10.3847/1538-4357/ac6f5a](https://doi.org/10.3847/1538-4357/ac6f5a)

Gaulme, P., & Guzik, J. A. 2019, Astronomy & Astrophysics, 630, A106, doi: [10.1051/0004-6361/201935821](https://doi.org/10.1051/0004-6361/201935821)

Giles, D. K., & Walkowicz, L. 2020, Monthly Notices of the Royal Astronomical Society, 499, 524, doi: [10.1093/mnras/staa2736](https://doi.org/10.1093/mnras/staa2736)

Guo, C., Pleiss, G., Sun, Y., & Weinberger, K. Q. 2017, On Calibration of Modern Neural Networks, arXiv, doi: [10.48550/arXiv.1706.04599](https://doi.org/10.48550/arXiv.1706.04599)

Harris, C. R., Millman, K. J., Van Der Walt, S. J., et al. 2020, Nature, 585, 357, doi: [10.1038/s41586-020-2649-2](https://doi.org/10.1038/s41586-020-2649-2)

He, K., Zhang, X., Ren, S., & Sun, J. 2015, Deep Residual Learning for Image Recognition, arXiv, doi: [10.48550/arXiv.1512.03385](https://doi.org/10.48550/arXiv.1512.03385)

Hendrycks, D., & Gimpel, K. 2018, A Baseline for Detecting Misclassified and Out-of-Distribution Examples in Neural Networks, arXiv, doi: [10.48550/arXiv.1610.02136](https://doi.org/10.48550/arXiv.1610.02136)

Hinners, T. A., Tat, K., & Thorp, R. 2018, The Astronomical Journal, 156, 7, doi: [10.3847/1538-3881/aac16d](https://doi.org/10.3847/1538-3881/aac16d)

Hon, M., Stello, D., & Yu, J. 2018a, Monthly Notices of the Royal Astronomical Society, 476, 3233, doi: [10.1093/mnras/sty483](https://doi.org/10.1093/mnras/sty483)

Hon, M., Stello, D., & Zinn, J. C. 2018b, The Astrophysical Journal, 859, 64, doi: [10.3847/1538-4357/aabfdb](https://doi.org/10.3847/1538-4357/aabfdb)

Howell, S. B., Sobeck, C., Haas, M., et al. 2014, Publications of the Astronomical Society of the Pacific, 126, 398, doi: [10.1086/676406](https://doi.org/10.1086/676406)

Hunter, J. D. 2007, Computing in Science & Engineering, 9, 90, doi: [10.1109/MCSE.2007.55](https://doi.org/10.1109/MCSE.2007.55)

Jamal, S., & Bloom, J. S. 2020a, The Astrophysical Journal Supplement Series, 250, 30, doi: [10.3847/1538-4365/aba8ff](https://doi.org/10.3847/1538-4365/aba8ff)

—. 2020b, The Astrophysical Journal Supplement Series, 250, 30, doi: [10.3847/1538-4365/aba8ff](https://doi.org/10.3847/1538-4365/aba8ff)

Jenkins, J. M., Twicken, J. D., McCauliff, S., et al. 2016, 9913, 99133E, doi: [10.1117/12.2233418](https://doi.org/10.1117/12.2233418)

Kessler, R., Narayan, G., Avelino, A., et al. 2019, Publications of the Astronomical Society of the Pacific, 131, 094501, doi: [10.1088/1538-3873/ab26f1](https://doi.org/10.1088/1538-3873/ab26f1)

Kluyver, T., Ragan-Kelley, B., Pérez, F., et al. 2016, in Positioning and Power in Academic Publishing: Players, Agents and Agendas, ed. F. Loizides & B. Schmidt (IOS Press), 87–90, doi: [10.3233/978-1-61499-649-1-87](https://doi.org/10.3233/978-1-61499-649-1-87)

Kohonen, T. 1990, Proceedings of the IEEE, 78, 1464, doi: [10.1109/5.58325](https://doi.org/10.1109/5.58325)

Liang, S., Li, Y., & Srikant, R. 2020, Enhancing The Reliability of Out-of-distribution Image Detection in Neural Networks, arXiv, doi: [10.48550/arXiv.1706.02690](https://doi.org/10.48550/arXiv.1706.02690)

Lightkurve Collaboration, Cardoso, J. V. d. M., Hedges, C., et al. 2018, Astrophysics Source Code Library, ascl:1812.013. <https://ui.adsabs.harvard.edu/abs/2018ascl.soft12013L>

Lin, T.-Y., Dollar, P., Girshick, R., et al. 2017, in Proceedings of the IEEE Conference on Computer Vision and Pattern Recognition, 2117–2125. [https://openaccess.thecvf.com/content\\_cvpr\\_2017/html/Lin\\_Feature\\_Pyramid\\_Networks\\_CVPR\\_2017\\_paper.html](https://openaccess.thecvf.com/content_cvpr_2017/html/Lin_Feature_Pyramid_Networks_CVPR_2017_paper.html)

Liu, J., Soria, R., Wu, X.-F., Wu, H., & Shang, Z. 2021a, Anais da Academia Brasileira de Ciencias, 93, 20200628, doi: [10.1590/0001-3765202120200628](https://doi.org/10.1590/0001-3765202120200628)

Liu, W., Wang, X., Owens, J. D., & Li, Y. 2021b, Energy-Based Out-of-distribution Detection, arXiv, doi: [10.48550/arXiv.2010.03759](https://doi.org/10.48550/arXiv.2010.03759)

Lomb, N. R. 1976, Astrophysics and Space Science, 39, 447, doi: [10.1007/BF00648343](https://doi.org/10.1007/BF00648343)

Malanchev, K. L., Pruzhinskaya, M. V., Korolev, V. S., et al. 2021, Monthly Notices of the Royal Astronomical Society, 502, 5147, doi: [10.1093/mnras/stab316](https://doi.org/10.1093/mnras/stab316)

Martínez-Galarza, J. R., Bianco, F. B., Crake, D., et al. 2021, Monthly Notices of the Royal Astronomical Society, 508, 5734, doi: [10.1093/mnras/stab2588](https://doi.org/10.1093/mnras/stab2588)

McInnes, L., Healy, J., & Melville, J. 2020, UMAP: Uniform Manifold Approximation and Projection for Dimension Reduction, arXiv, doi: [10.48550/arXiv.1802.03426](https://doi.org/10.48550/arXiv.1802.03426)

Microsoft Corporation. 2023, Azure OpenAI Service, Microsoft Corporation. <https://azure.microsoft.com/en-us/products/ai-services/openai-service>

Mishkin, D., Sergievskiy, N., & Matas, J. 2017, Computer Vision and Image Understanding, 161, 11, doi: [10.1016/j.cviu.2017.05.007](https://doi.org/10.1016/j.cviu.2017.05.007)

Möller, A., & de Boissière, T. 2020, Monthly Notices of the Royal Astronomical Society, 491, 4277, doi: [10.1093/mnras/stz3312](https://doi.org/10.1093/mnras/stz3312)

Mowlavi, N., Lecoeur-Taïbi, I., Lebzelter, T., et al. 2018, Astronomy & Astrophysics, 618, A58, doi: [10.1051/0004-6361/201833366](https://doi.org/10.1051/0004-6361/201833366)

Muthukrishna, D., Narayan, G., Mandel, K. S., Biswas, R., & Hložek, R. 2019, Publications of the Astronomical Society of the Pacific, 131, 118002, doi: [10.1088/1538-3873/ab1609](https://doi.org/10.1088/1538-3873/ab1609)

Naeini, M. P., Cooper, G. F., & Hauskrecht, M. 2015, Proceedings of the ... AAAI Conference on Artificial Intelligence. AAAI Conference on Artificial Intelligence, 2015, 2901. <https://www.ncbi.nlm.nih.gov/pmc/articles/PMC4410090/>

Naul, B., Bloom, J. S., Pérez, F., & van der Walt, S. 2018, Nature Astronomy, 2, 151, doi: [10.1038/s41550-017-0321-z](https://doi.org/10.1038/s41550-017-0321-z)

Neubeck, A., & Van Gool, L. 2006, in 18th International Conference on Pattern Recognition (ICPR'06), Vol. 3, 850–855, doi: [10.1109/ICPR.2006.479](https://doi.org/10.1109/ICPR.2006.479)

Niculescu-Mizil, A., & Caruana, R. 2005, in Proceedings of the 22nd International Conference on Machine Learning, ICML '05 (New York, NY, USA: Association for Computing Machinery), 625–632, doi: [10.1145/1102351.1102430](https://doi.org/10.1145/1102351.1102430)

OpenAI. 2023, GPT-4 Technical Report, doi: [10.48550/arXiv.2303.08774](https://doi.org/10.48550/arXiv.2303.08774)

Ouyang, L., Wu, J., Jiang, X., et al. 2022, Training Language Models to Follow Instructions with Human Feedback, arXiv, doi: [10.48550/arXiv.2203.02155](https://doi.org/10.48550/arXiv.2203.02155)

Pan, J.-S., Ting, Y.-S., & Yu, J. 2023, Astroconformer: The Prospects of Analyzing Stellar Light Curves with Transformer-Based Deep Learning Models, doi: [10.48550/arXiv.2309.16316](https://doi.org/10.48550/arXiv.2309.16316)

Pasquet, J., Pasquet, J., Chaumont, M., & Fouchez, D. 2019, *Astronomy and Astrophysics*, 627, A21, doi: [10.1051/0004-6361/201834473](https://doi.org/10.1051/0004-6361/201834473)

Paszke, A., Gross, S., Massa, F., et al. 2019, in *Advances in Neural Information Processing Systems*, Vol. 32 (Curran Associates, Inc.).  
[https://papers.nips.cc/paper\\_files/paper/2019/hash/bdbca288fee7f92f2bfa9f7012727740-Abstract.html](https://papers.nips.cc/paper_files/paper/2019/hash/bdbca288fee7f92f2bfa9f7012727740-Abstract.html)

Pimentel, Ó., Estévez, P. A., & Förster, F. 2022, *The Astronomical Journal*, 165, 18, doi: [10.3847/1538-3881/ac9ab4](https://doi.org/10.3847/1538-3881/ac9ab4)

Prša, A., Batalha, N., Slawson, R. W., et al. 2011, *The Astronomical Journal*, 141, 83, doi: [10.1088/0004-6256/141/3/83](https://doi.org/10.1088/0004-6256/141/3/83)

Pruzhinskaya, M. V., Malanchev, K. L., Kornilov, M. V., et al. 2019, *Monthly Notices of the Royal Astronomical Society*, 489, 3591, doi: [10.1093/mnras/stz2362](https://doi.org/10.1093/mnras/stz2362)

Ren, S., He, K., Girshick, R., & Sun, J. 2016, Faster R-CNN: Towards Real-Time Object Detection with Region Proposal Networks, arXiv, doi: [10.48550/arXiv.1506.01497](https://doi.org/10.48550/arXiv.1506.01497)

Ricker, G. R., Winn, J. N., Vanderspek, R., et al. 2014, *Journal of Astronomical Telescopes, Instruments, and Systems*, 1, 014003, doi: [10.1111/1.JATIS.1.1.014003](https://doi.org/10.1111/1.JATIS.1.1.014003)

Sánchez-Sáez, P., Reyes, I., Valenzuela, C., et al. 2021, *The Astronomical Journal*, 161, 141, doi: [10.3847/1538-3881/abd5c1](https://doi.org/10.3847/1538-3881/abd5c1)

Sánchez-Sáez, P., Arredondo, J., Bayo, A., et al. 2023, *Astronomy and Astrophysics*, 675, A195, doi: [10.1051/0004-6361/202346077](https://doi.org/10.1051/0004-6361/202346077)

Scargle, J. D. 1982, *The Astrophysical Journal*, 263, 835, doi: [10.1086/160554](https://doi.org/10.1086/160554)

Shao, F., Chen, L., Shao, J., et al. 2021, Deep Learning for Weakly-Supervised Object Detection and Object Localization: A Survey.  
<https://arxiv.org/abs/2105.12694v1>

Shappee, B. J., Prieto, J. L., Grupe, D., et al. 2014, *The Astrophysical Journal*, 788, 48, doi: [10.1088/0004-637X/788/1/48](https://doi.org/10.1088/0004-637X/788/1/48)

Smith, J. C., Stumpe, M. C., Cleve, J. E. V., et al. 2012, *Publications of the Astronomical Society of the Pacific*, 124, 1000, doi: [10.1086/667697](https://doi.org/10.1086/667697)

Sun, F.-K., & Boning, D. S. 2022, FreDo: Frequency Domain-based Long-Term Time Series Forecasting, arXiv, doi: [10.48550/arXiv.2205.12301](https://doi.org/10.48550/arXiv.2205.12301)

Sun, Y., & Li, Y. 2022, DICE: Leveraging Sparsification for Out-of-Distribution Detection, arXiv, doi: [10.48550/arXiv.2111.09805](https://doi.org/10.48550/arXiv.2111.09805)

The Astropy Collaboration, Robitaille, T. P., Tollerud, E. J., et al. 2013, *Astronomy & Astrophysics*, 558, A33, doi: [10.1051/0004-6361/201322068](https://doi.org/10.1051/0004-6361/201322068)

The Astropy Collaboration, Price-Whelan, A. M., Sipőcz, B. M., et al. 2018, *The Astronomical Journal*, 156, 123, doi: [10.3847/1538-3881/aabc4f](https://doi.org/10.3847/1538-3881/aabc4f)

Twicken, J. D., Catanzarite, J. H., Clarke, B. D., et al. 2018, *Publications of the Astronomical Society of the Pacific*, 130, 064502, doi: [10.1088/1538-3873/aab694](https://doi.org/10.1088/1538-3873/aab694)

van der Maaten, L., & Hinton, G. 2008, *Journal of Machine Learning Research*, 9, 2579.  
<http://jmlr.org/papers/v9/vandermaaten08a.html>

Villar, V. A., Cranmer, M., Berger, E., et al. 2021, *The Astrophysical Journal Supplement Series*, 255, 24, doi: [10.3847/1538-4365/ac0893](https://doi.org/10.3847/1538-4365/ac0893)

Villar, V. A., Berger, E., Miller, G., et al. 2019, *The Astrophysical Journal*, 884, 83, doi: [10.3847/1538-4357/ab418c](https://doi.org/10.3847/1538-4357/ab418c)

Vovk, V., Gammerman, A., & Saunders, C. 1999, in *Proceedings of the Sixteenth International Conference on Machine Learning, ICML '99* (San Francisco, CA, USA: Morgan Kaufmann Publishers Inc.), 444–453

Wang, H., Li, Z., Feng, L., & Zhang, W. 2022, ViM: Out-Of-Distribution with Virtual-logit Matching, arXiv, doi: [10.48550/arXiv.2203.10807](https://doi.org/10.48550/arXiv.2203.10807)

Yang, J., Zhou, K., Li, Y., & Liu, Z. 2022, Generalized Out-of-Distribution Detection: A Survey, arXiv, doi: [10.48550/arXiv.2110.11334](https://doi.org/10.48550/arXiv.2110.11334)

Yang, Z., Luo, T., Wang, D., et al. 2018, Learning to Navigate for Fine-grained Classification, arXiv, doi: [10.48550/arXiv.1809.00287](https://doi.org/10.48550/arXiv.1809.00287)

Yu, J., Bedding, T. R., Stello, D., et al. 2020, *Monthly Notices of the Royal Astronomical Society*, 493, 1388, doi: [10.1093/mnras/staa300](https://doi.org/10.1093/mnras/staa300)

Zeiler, M. D., & Fergus, R. 2014, in *Computer Vision – ECCV 2014*, ed. D. Fleet, T. Pajdla, B. Schiele, & T. Tuytelaars, *Lecture Notes in Computer Science* (Cham: Springer International Publishing), 818–833, doi: [10.1007/978-3-319-10590-1\\_53](https://doi.org/10.1007/978-3-319-10590-1_53)

Zeng, A., Chen, M., Zhang, L., & Xu, Q. 2022, Are Transformers Effective for Time Series Forecasting?, arXiv, doi: [10.48550/arXiv.2205.13504](https://doi.org/10.48550/arXiv.2205.13504)